Chapter 2
Averaging Methods for Computational Micromechanics

The averaging or homogenization process is the foundation of all unit cell models and any yield criterion derived from them. In porous materials, the presence of a void gives rise to an overall response of the bulk or aggregate material that is different than that of a damage-free material. The averaging process is employed to transition from the micro-scale (unit-cell) to the macro-scale to quantify the overall response of the material and these average quantities are frequently referred to as "macroscopic" quantities. The study of homogenization techniques is a very rich field and a proper treatment is outside the scope of this book and the interested reader is referred to basic textbooks on plasticity as well as the work of Eshelby (1957), Mori and Tanaka (1973), Nemat-Nasser (1993a, b) as well as Ponte Casteneda and Suquet (1998). Only a brief explanation of the extremum theory of plasticity is provided here since a great deal of attention will be paid to the application of upper and lower bound-based yield criteria for porous ductile materials.

2.1 Defination of Average Stress and Strain

Consider an arbitrary representative volume element (RVE) or unit cell that is large enough to statistically represent the material behaviour of the aggregate material. For an arbitrary unit cell geometry, the macroscopic stresses are obtained as the volume average of the microscopic stresses as

$$\Sigma_{ij} = \frac{1}{V}\int_V \sigma_{ij}(\boldsymbol{x})dV \tag{2.1}$$

where $\sigma_{ij}(x)$ are the micro-stress fields in a unit cell at a point, $\boldsymbol{x}$; Σ_{ij} is the macroscopic stress tensor and V is the volume of the unit cell. This integral can be converted to an integration of the applied surface traction vector, $T_i(x)$, over the outer boundary of the unit cell, S, using the Gauss theorem

Z. Chen and C. Butcher, *Micromechanics Modelling of Ductile Fracture*,
Solid Mechanics and Its Applications 195, DOI 10.1007/978-94-007-6098-1_2,

$$\Sigma_{ij} = \frac{1}{V}\int_V \sigma_{ij}(x)dV = \frac{1}{S}\int_S T_i(x)n_j dS \tag{2.2}$$

where n_j are the components of surface normal direction vector corresponding to $T_i(x)$. The average strain rate fields are similarly defined as

$$\dot{E}_{ij} = \frac{1}{V}\int_V \dot{\varepsilon}_{ij}(x)dV = \frac{1}{V}\int_S \frac{1}{2}\left[v_i(x)n_j + v_j(x)n_i\right]dS \tag{2.3}$$

where $\dot{\varepsilon}_{ij}$ and $\dot{E}_{ij}$ are the respective microscopic and macroscopic strain rates and v_i are the components of the velocity vector on the outer surfaces of the unit cell. The average work rate is thus defined by

$$\dot{W} = \frac{1}{V}\int_V \sigma_{ij}\dot{\varepsilon}_{ij}dV = \frac{1}{V}\int_S T_i v_i dS = \Sigma_{ij}\dot{E}_{ij} \tag{2.4}$$

Based on the energy Eq. (2.4) and the variational method, the stress strain relation can be obtained using the following equations

$$\dot{E}_{ij} = \frac{\partial \dot{W}}{\partial \Sigma_{ij}} \tag{2.5}$$

$$\Sigma_{ij} = \frac{\partial \dot{W}}{\partial \dot{E}_{ij}} \tag{2.6}$$

2.2 Fundamentals of a Constitutive Model for Plasticity

The constitutive equation of a material is used to relate the material response (stress) to an applied deformation (strain). The constitutive equation, or plastic potential, ϕ, is a scalar function of the stress tensor along with some internal variables arranged in a vector, α. The general form of the plastic potential for a perfectly plastic material is expressed as

$$\phi\left(\sigma_{ij}, \alpha_i\right) = \sigma_0 \tag{2.7}$$

From the concept of the plastic potential (Chakrabarty 1987), the microscopic plastic strain increment, $d\varepsilon_{ij}$, is related to the normal of the yield surface with a scalar factor known as the plastic multiplier, $d\lambda$, and thus defines the "flow rule" of the material as

$$d\varepsilon_{ij}^{p} = d\lambda \frac{\partial \phi(\sigma_{ij}, \alpha_i)}{\partial \sigma_{ij}} \tag{2.8}$$

This is known as an associated flow rule because the plastic potential is the same as the yield criterion. Non-associated flow rules can also be implemented but are not considered in this book.

2.3 Normality and Convexity of the Yield Surface

The fundamentals of the mathematical theory of plasticity require that the yield surface be convex since the work dissipation for a deforming material is always positive. They also constitute the basis for many minimum/maximum theorems in plasticity, including the upper- and lower-bound theorems to be discussed and utilized throughout this book. The condition of normality is fundamental to the development of the plastic flow rule since the vector of the plastic strain increment is always normal to the yield surface. The convexity condition forms the basis of the principle of maximum plastic work. Taking the yield locus as an example, convexity can be formulated as

$$(\Sigma_1 - \Sigma_2) : \left(\frac{\partial \Phi}{\partial \Sigma}\right)_{\Sigma_1} \geq \Phi(\Sigma_1) - \Phi(\Sigma_2) \tag{2.9}$$

where Σ_1 and Σ_2 indicate two different macroscopic stress tensors and $\Phi(\Sigma, \alpha)$ is the macroscopic plastic potential.

2.4 Principle of Virtual Work

A stress field can be said to be statically admissible if it satisfies the equilibrium equations

$$\frac{\partial \sigma_{ij}}{\partial x_i} = 0 \tag{2.10}$$

If we consider an admissible velocity field, v_i, to be independent of the equilibrium stress field, the work rate done by the surface tractions and its volume-based equivalent are

$$\int T_i v_i dS = \int n_i \sigma_{ij} v_i dS \tag{2.11}$$

$$\int n_i \sigma_{ij} v_i dS = \int \sigma_{ij} \frac{\partial v_i}{\partial x_j} dV = \int \sigma_{ij} \dot{\varepsilon}_{ij} dV \tag{2.12}$$

Equations (2.11) and (2.12) define the principle of virtual work which states that the rate of work done by the surface tractions with any virtual velocity field is equal to the rate of dissipation of internal energy by the stress field corresponding to the surface tractions

$$\int T_i v_i dS = \int \sigma_{ij} \dot{\varepsilon}_{ij} dV \tag{2.13}$$

2.5 Principle of Maximum Plastic Work

The work rate of plastic deformation is

$$dW = \sigma_{ij} d\varepsilon_{ij} \tag{2.14}$$

For a given plastic strain increment, $d\varepsilon_{ij}^p$, the corresponding stress σ_{ij}, can be determined from the normality rule and the yield function and denoted as point P in stress space. Now consider an arbitrary stress, σ_{ij}^*, that is statically admissible and denoted by a point P^* that lies on or inside the yield surface. From the principle of virtual work, the difference between the incremental plastic works done by the two stresses can be determined as follows

$$dW = \left(\sigma_{ij} - \sigma_{ij}^*\right) d\varepsilon_{ij}^p \tag{2.15}$$

since the yield surface is strictly convex the scalar product is positive. Hence,

$$dW = \left(\sigma_{ij} - \sigma_{ij}^*\right) d\varepsilon_{ij}^p \geq 0 \tag{2.16}$$

Equation (2.16) represents the principle of maximum plastic work: the actual work done in a given plastic strain increment is greater than or equal to the work done by an arbitrary stress that is less than or equal to the yield limit.

2.6 Extremum Theorems in Plasticity

The extremum principles in plasticity arise from the comparison of the work dissipations (or work rates) associated with actual stress fields and velocity fields. A lower bound estimate can be obtained by applying a statically admissible stress

field at the cell boundary while an upper bound estimate is obtained by applying a kinematically admissible velocity field. The principle of virtual work is used to obtain the difference between the actual and possible fields.

For a mass of material with a volume, V and bounded by a surface S, the equation of energy conservation is

$$\int T_i v_i dS = \int \sigma_{ij} \dot{\varepsilon}_{ij} dV + \int \tau [v] dS_D \tag{2.17}$$

where S_D is the surface on which a discontinuity of velocity occurs and τ and $[v]$ are the shear stress and relative velocity on the dislocation surface S_D (Kachanov 1971). Equation (2.17) holds for any continuous medium in equilibrium and the velocities and stresses are, in general, not related. In other words, Eq. (2.17) is applicable to both the actual stress distribution σ_{ij} and to any kinematically possible velocity field v_i^*; it is also applicable to both to the actual velocity distribution v_i and a statically admissable stress field, σ_{ij}^*.

2.6.1 Upper Bound Solution

According to Kachanov (1974), the upper bound principle states that the total rate of work attains an absolute minimum for the actual velocity field when

$$\int T_i^* v_i dS \geq \int T_i v_i dS \tag{2.18}$$

where T_i^* are surface tractions solutions corresponding to any kinematically possible velocity fields v_i. Upper bound yield functions for porous materials can be obtained by constructing a uniform velocity field on the outer surface of a unit cell. The upper bound theorem is used to solve for the forces that arise due to deformation from a kinematically possible velocity field. In general, upper bound solutions are easier to obtain analytically because they represent solving for the stress (load) from an applied strain (deformation).

2.6.2 Lower Bound Solution

As stated by Kachanov (1974): the rate of work done by the actual surface tractions on prescribed velocities is greater than or equal to the rate of work developed by surface tractions corresponding to any statically admissible stress

$$\int T_i^* v_i dS \leq \int T_i v_i dS \tag{2.19}$$

where T_i^* are obtained from any statically admissible microscopic stress fields. Lower bound yield limits for porous materials can be obtained by constructing stress fields instead of velocity fields. Theoretically, the yield strength obtained using a yield criterion derived using the lower bound formulation will always be lower than the real yield stress.

2.7 Gurson's Upper Bound Solution for a Porous Ductile Material

Some of the earliest work in modelling damage-induced ductile fracture was performed by McClintock (1968) who studied the axisymmetric deformation of an infinitely long circular-cylindrical void in an infinite, perfectly plastic matrix material. Rice and Tracey (1969) considered the same problem but for the growth of an initially spherical void. It is important to mention that while these studies related the void growth and evolution to the far-field loading, the bulk behaviour of the material was independent of the void damage. Building upon the work of Green (1972) and the numerical results of Needleman (1972) for a cylindrical unit cell, Gurson (1977) derived a damage-based yield criterion and flow rules for both cylindrical and spherical unit cells. In this model, the macroscopic response of the material is directly linked to the porosity and its evolution. The Gurson model is based on upper bound plasticity theory and thus the model will overestimate the material strength and underestimate the porosity in the material by restricting void growth.

To simplify the analysis, the Gurson-based material is assumed to have a periodic distribution of voids with each void located at the centre of a cylindrical or spherical unit cell. In this manner, the randomly distributed voids in the material are replaced with an equivalent single void. In reality, the void distribution is random with voids and particles of many sizes as shown in Fig. 1.11. The unit cells used by Gurson are only approximations to a periodic microstructure because the assembling of the unit cells to represent the bulk material will neglect the material between the cells (Fig. 2.1). These approximations of the unit cell geometries are required to simplify the problem so that a closed-form yield criterion can be derived. Twenty years later, Gologanu et al. (1997) followed a similar approach as Gurson but considered ellipsoidal voids embedded in an ellipsoidal unit cell so that the evolution of the void shape and shape-induced anisotropy could be captured. To maintain the integrity of the presentation, the definition of porosity in the Gurson unit cells is repeated here

$$\text{Spherical: } f = \frac{a^3}{b^3} \qquad \text{Cylindrical: } f = \frac{a^2}{b^2} \tag{1.21a, b}$$

where a is the radius of the void and b the radius of the unit cell.

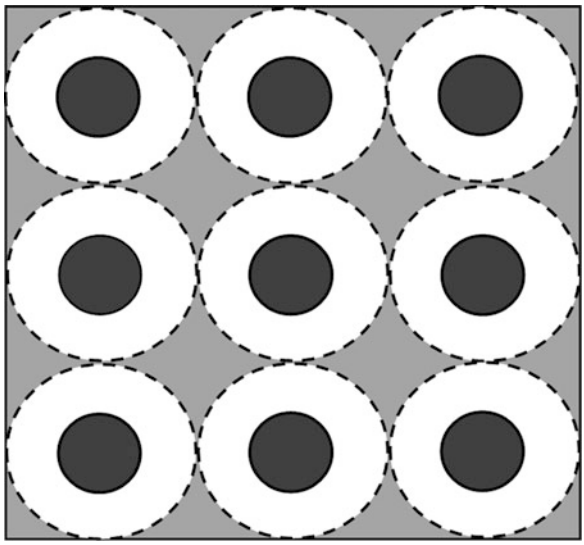

Fig. 2.1 Top-view of a material composed of a periodic array of spherical or cylindrical unit cells. Note the material that is not included in the homogenization process for these cell geometries

Another advantage of Gurson's model is its implicit accounting for material isotropy as the voids are assumed to remain spherical or cylindrical. The spherical model is geometrically isotropic while the cylindrical void experiences transverse isotropy. Gurson's yield criteria for spherical and cylindrical voids are

$$\text{Spherical void: } \Phi = \frac{\Sigma_{\text{eq}}^2}{\bar{\sigma}^2} + 2f\cosh\left(\frac{3}{2}\frac{\Sigma_{\text{hyd}}}{\bar{\sigma}}\right) - 1 - f^2 = 0 \tag{2.20a}$$

$$\text{Cylindrical void: } \Phi = \frac{\Sigma_{\text{eq}}^2}{\bar{\sigma}^2} + 2f\cosh\left(\frac{3\sqrt{3}}{2}\frac{\Sigma_{\text{hyd}}}{\bar{\sigma}}\right) - 1 - f^2 = 0 \tag{2.20b}$$

where $\bar{\sigma}$ is the equivalent tensile flow stress in the matrix material, neglecting variations in local stress, and Σ_{eq} and Σ_{hyd} are the macroscopic effective and hydrostatic stresses, respectively. Gurson's formulation reduces to the von Mises yield criterion for a damage free material by setting $f = 0$ in Eq. (2.20). The relationship between Gurson's damage model and the von Mises criterion with hydrostatic stress is presented in Fig. 2.2. The von Mises criterion is independent of the hydrostatic stress because it is assumed to be free of interal defects (voids, particles, inclusions) and because a hydrostatic stress will not induce any shear stresses. Damage-based materials are sensitive to the hydrostatic stress because a tensile hydrostatic stress will expand the voids, softening the material and resulting in earlier necking and failure. Conversely, a compressive hydrostatic stress will increase formability by shrinking the size of the voids.

The spherical void variant of the Gurson model was well-received but it was soon realized that it provided an overly stiff response when compared to the numerical

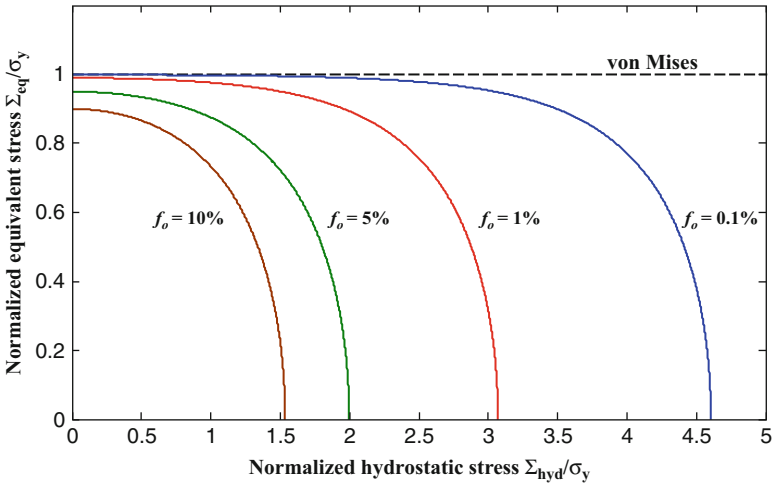

Fig. 2.2 Gurson (1977) yield function showing the reduction in the macroscopic equivalent stress with increasing hydrostatic stress and porosity

solutions of porous materials. Tvergaard (1981) extended Gurson's model to account for shear band instabilities and introduced three calibration parameters, q_1, q_2 and q_3 to better match the effects of voids during plastic deformation. The q_i parameters serve to artificially soften the material response and encourage void growth. Traditionally, the parameters are assumed to be material constants with $q_1 \approx 1.25 - 1.5$, $q_2 \approx 1$ and $q_3 = {q_1}^2$ based on the numerical work of Koplik and Needleman (1988). Other researchers such as Faleskog and Shih (1997) and Ragab (2004a) have proposed correlations for the q_i parameters as functions of the stress state, void shape and material properties and generally $q_1 \geq 1$ and $q_2 \leq 1$. The variation of the yield surfaces with the q_1 and q_2 parameters are shown in Figs. 2.3 and 2.4. The modification of Tvergaard forms the Gurson-Tvergaard (GT) model and has become the standard formulation of the Gurson yield surface.

2.7.1 Void Growth and Nucleation

The effects of void nucleation and void growth must be included to model damage evolution in a material. Void nucleation and growth are considered independently and damage development is expressed as the sum of these effects

$$\dot{f} = \dot{f}_{\text{growth}} + \dot{f}_{\text{nucleation}} \tag{2.21}$$

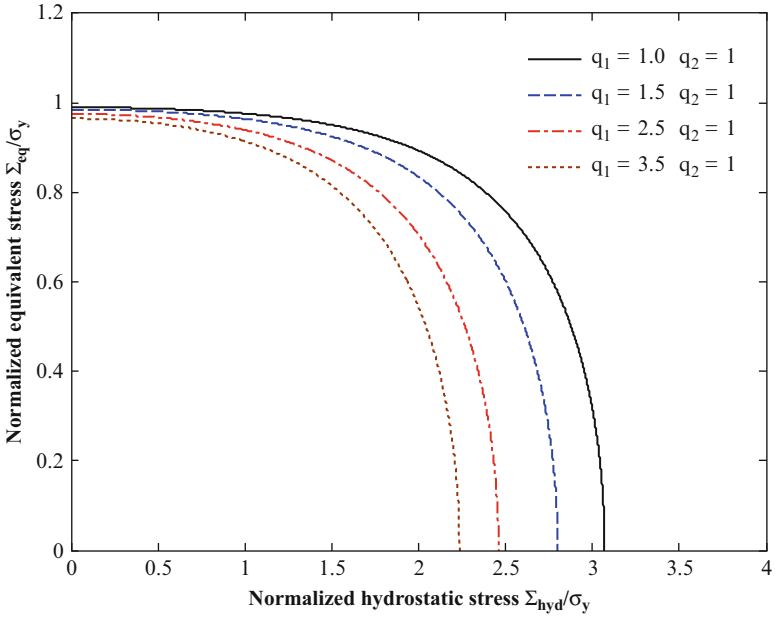

Fig. 2.3 Varation of the Gurson-Tvergaard yield surface with the q_1 parameter for a porosity of 1 %

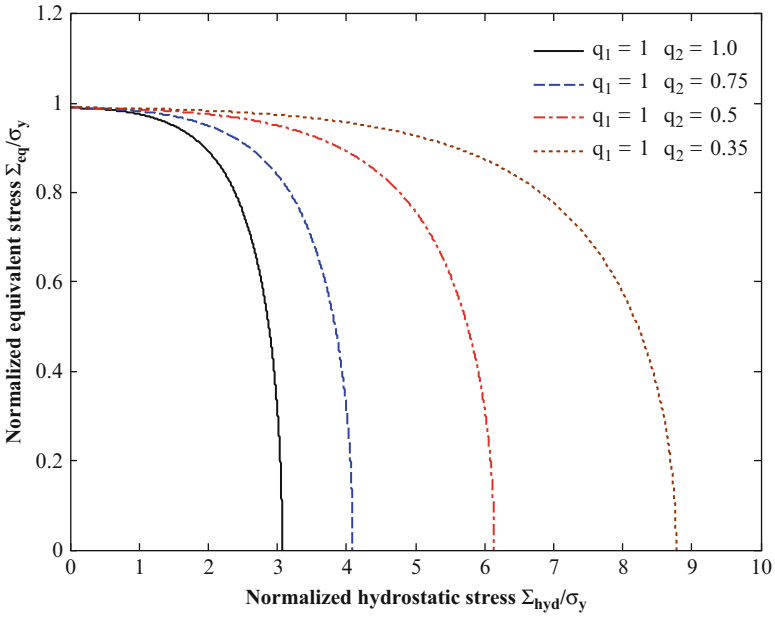

Fig. 2.4 Variation of the Gurson-Tvergaard yield surface with the q_2 parameter for a porosity of 1 %

The growth rate of the voids is proportional to the plastic volume dilatation rate

$$\dot{f}_{\text{growth}} = 3(1-f)\dot{\varepsilon}^{p}_{\text{hyd}} \tag{2.22}$$

where $\dot{\varepsilon}^{p}_{\text{hyd}}$ is the hydrostatic component of the plastic strain increment. The void growth equation in Eq. (2.22) is valid for all other damage-based constitutive models but the void growth rate will be different since $\dot{\varepsilon}^{p}_{\text{hyd}}$ is related to the shape of the yield surface through the associated flow rule:

$$\dot{\varepsilon}^{p}_{\text{hyd}} = d\lambda \cdot \frac{\partial \Phi}{\partial \sigma_{\text{hyd}}} \tag{2.23}$$

As discussed previously, void nucleation can be stress or strain-controlled. A review of the commonly used nucleation models can be found in Chap. 1.

2.7.2 Void Coalescence

The majority of work on void coalescence has been investigated using Gurson-based constitutive models because void growth, nucleation and material softening are included. However, the Gurson (1977) model is not particularly useful as a fracture criterion since material softening is a continuous process with a complete loss of material strength occurring when the porosity reaches 100 %. Obviously, this is unrealistic and a complete loss of load carrying capacity in a material occurs at porosities on the order of several percent. The introduction of the q_{i} parameters reduced the porosity at fracture to $1/q_1$ or between 66.7 and 100 %, depending on the value of q_1, but it was not sufficient to bring the model prediction closer to the reality.

2.7.2.1 Critical Porosity Coalescence Model

To address the unrealistic fracture porosities in the GT model, Tvergaard and Needleman (1984) proposed a phenomenological coalescence model that relies upon a critical porosity to identify the onset of coalescence and failure. In this approach, once the specified "critical porosity" has been reached, the porosity is rapidly increased to simulate the sudden drop in load carrying capacity associated with ductile fracture (see Fig. 2.5). The resulting criterion uses an effective porosity term, f^*, that replaces the original porosity term in the GT yield criterion:

$$f^* = \begin{cases} f & \text{if } f \le f_{\text{c}} \\ f_{\text{c}} + \dfrac{f_{\text{u}}{}^* - f}{f_{\text{f}} - f_{\text{c}}}(f - f_{\text{c}}) & \text{if } f \ge f_{\text{c}} \end{cases} \tag{2.24}$$

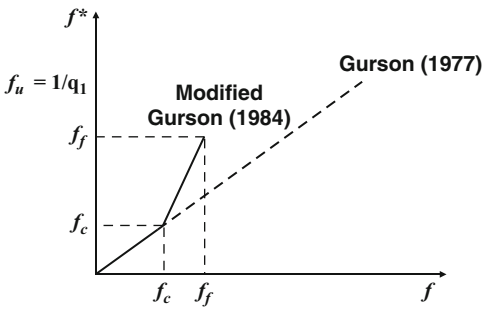

Fig. 2.5 Qualitative sketch of Tvergaard and Needleman's modification to simulate coalescence and rapid loss of material strength (Reprinted with permission from Zhang (1998). Copyright 1998 WIT Press Southampton)

where f_c is the critical porosity. Void nucleation, growth and coalescence continue to until the failure porosity is reached, f_f, where all material strength vanishes. The ultimate porosity, f_u^*, has no physical significance and is equal to $1/q_1$. The critical void volume fraction and porosity at failure were initially assumed to be universal constants with values of 0.15 and 0.25, respectively. This variant of the model is commonly referred to as the GTN model (Gurson-Tvergaard-Needleman) and is the most widely used variant of the Gurson model.

The value of f_f controls the rate that the load carrying capacity is lost with a smaller failure porosity corresponding to a steeper load drop prior to fracture. One method to identify the value of f_f is to best match the experimental drop in load carrying capacity from a tension test. It is important to note that the value of f_f does not play a significant role in numerical modeling once the critical porosity, f_c is determined and if f_f is kept the same during fitting (Zhang and Niemi 1994a, b). For practical sheet metal forming operations where the triaxiality (ratio of the hydrostatic-to-effective stress) is low (less than 1), the post-coalescence regime is not significant with a negligible difference between the coalescence and fracture strains (Scheyvaerts et al. 2010).

Numerical simulations of voided unit cells show that the phemenological post-coalescence response in Eq. (2.24) can accurately describe the material response since the porosity and the corresponding load drop behave in a linear fashion as shown in Figs. 2.6 and 2.7.

Becker (1987) applied the GTN model to investigate the effect of porosity distribution on the ductile fracture of a porous iron compact. Becker observed that the critical and final porosities were not universal constants among different materials and suggested values of $f_c = 0.075$ and $f_f = 0.09$ for the model material. Koplik and Needleman (1988) agreed with Becker's conclusion that the critical porosity is related to initial porosity and stress triaxiality and suggested that f_c should instead be specified as a material constant. To determine f_c for a given material, the value of f_c is taken that best fits the load drop point in a tension test (Sun et al. 1989) or from microscopy of the fracture surface. The critical porosity can also be determined using a unit cell model (Koplik and Needleman 1988) but it will still be challenging to match the experimental value.

Nowadays, it is universally recoginized that the critical porosity is not a material constant since it is a function of the initial porosity, void shape, stress state and

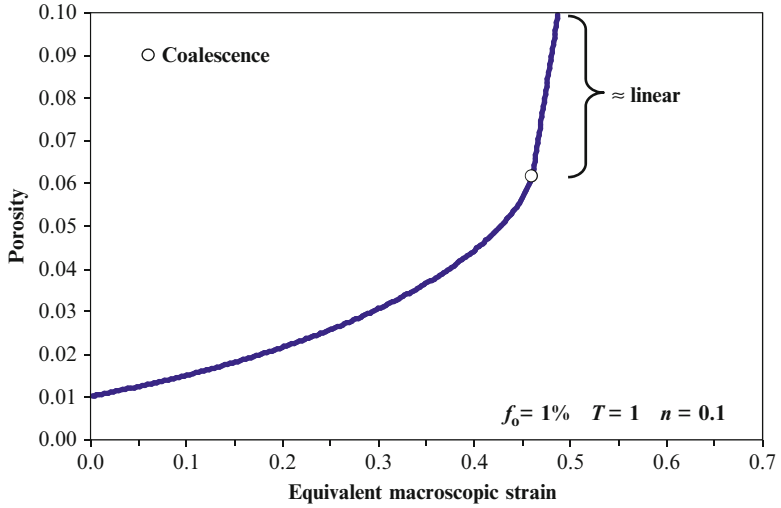

Fig. 2.6 Porosity evolution in an axisymmetric unit cell containing an initially spherical void

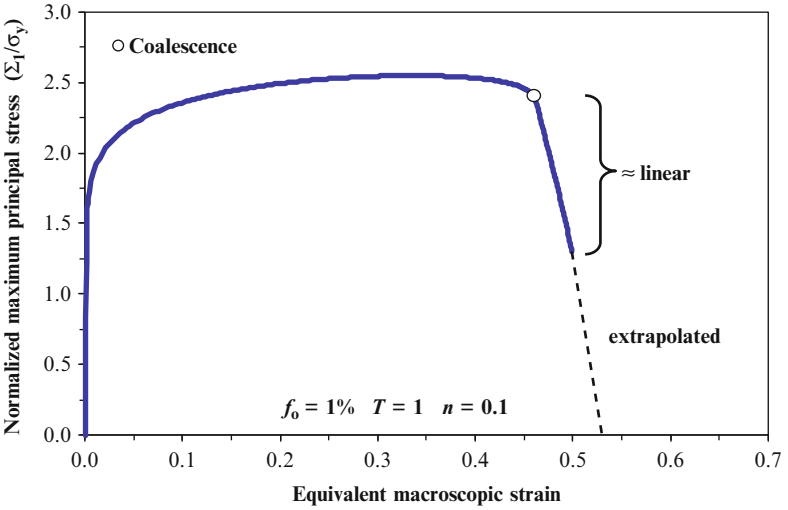

Fig. 2.7 Macroscopic stress response in an axisymmetric unit cell containing an initially spherical void

material properties (Zhang and Niemi 1994a; Pardoen and Delannay 1998b; Pardoen and Hutchinson 2000; Zhang et al. 2000). The variation of the critical porosity with the void shape and stress triaxiality obtained from unit cell simulations is presented in Fig. 2.8. From this figure, it is clearly shown that the

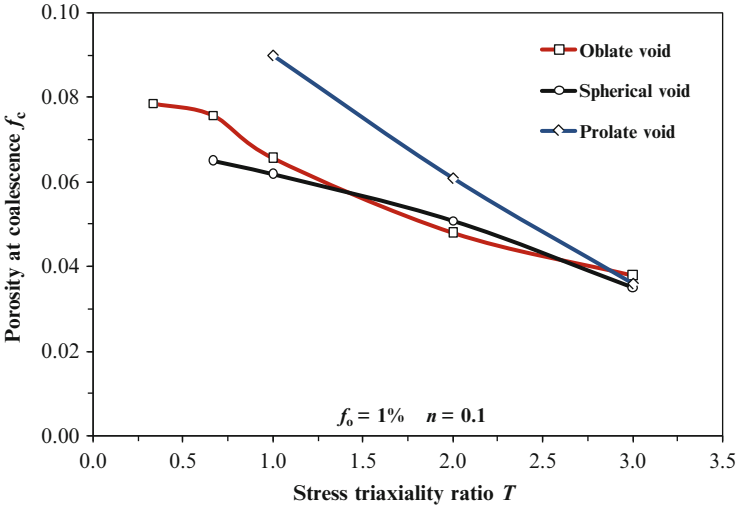

Fig. 2.8 Variation of the porosity at coalescence with the stress triaxiality and initial void shape. The aspect ratio of the oblate void is 1/6 and the aspect ratio of the prolate void is 6. The coalescence porosities were obtained from finite-element simulations of an axisymmetric unit cell

critical porosity model is reasonable at high stress triaxialities which is the intended regime for the Gurson model. The GTN model is well suited for fracture mechanics and applications related to crack propagation since the stress triaxiality ahead of a crack tip is high enough for the voids to grow in an approximately spherical manner. The critical porosity coalescence model is still in use today because it is available in commercial finite-element codes and some researchers have previously characterized the f_c value for their materials of interest. However, the reader is cautioned that this coalescene model should only be used for a well-defined material and that the critical porosity determined in one stress state will likely not be valid in a different application.

Fortunately, the critical porosity coalescence model has largely been supplanted by the plastic limit-load criterion of Thomason (1990) that describes the necking failure of the inter-void ligaments. In this physically-motivated model, void coalescence is a function of the stress state and the microstructure geometry with f_c becoming a field quantity. By removing f_c as a material constant, the nucleation parameters can be determined from tensile tests, instead of being pre-assumed in order to determine f_c by calibration with experiments. This is a significant improvement for Gurson-based models as the nucleation parameters can be easily determined and contains a fracture criterion based on the physical mechanism of coalescence.

2.7.2.2 Plastic Limit-Load Coalescence Criterion

To account for the physical mechanism of void coalescence, Thomason (1985a, b, 1990) theorized coalescence as the competition between stable homogeneous and

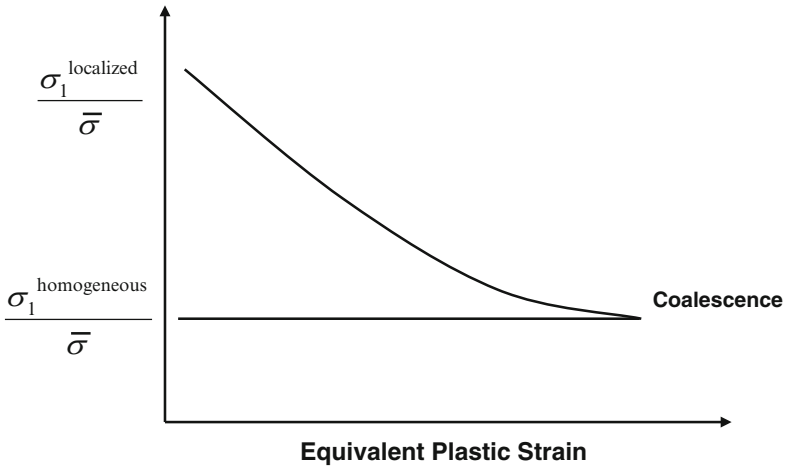

Fig. 2.9 Qualitative sketch of competing deformation modes as envisaged by Zhang (1998)

unstable localized deformation modes. Initially, the influence of voids is small and the deformation mode is homogenous. As voids nucleate and grow during further plastic deformation, the energy required to achieve an unstable localized deformation mode decreases. The point at which the homogenous and localized deformation modes become equal is taken as the onset of void coalescence and localized deformation as shown in Fig. 2.9. At this point, the plastic limit of the inter-void ligament has been reached and internal necking of the matrix begins, resulting in sudden localized fracture.

Zhang and Niemi (1994b) modified Thomason's plastic limit-load criterion to incorporate it into the Gurson-Tvergaard-Needleman (GTN) constitutive model to form the so-called complete Gurson model (CGM). More recently, Zhang et al. (2000) further extended his model to include the effect of hardening. In the modified plastic limit-load criterion, the voids are assumed to remain spherical and the constraint factor is expressed as

$$C_{f-Z} = (0.12 + 1.68n)\left(\chi^{-1} - 1\right)^2 + 1.24\chi^{-1/2} \tag{2.25a,b}$$

where n is the hardening exponent and χ is the void spacing ratio that is defined for spherical voids as

$$\chi = \left(\frac{f}{\gamma_{\text{cell}}} e^{\frac{3}{2}\left(\varepsilon_1 - \varepsilon_{\text{hyd}}\right)}\right)^{1/3} \qquad \gamma_{\text{cell}} = \begin{cases} 2/3 \text{ cylindrical unit cell} \\ \pi/6 \text{ cubic unit cell} \end{cases} \tag{2.26a,b}$$

where $\left(\varepsilon_1 - \varepsilon_{\text{hyd}}\right)_c$ is the principal deviatoric strain. The variants of the plastic limit-load models by Pardoen and Hutchinson (2000) and Benzerga (2002) found in Eqs. (1.15) and (1.16) could also be employed by setting the aspect ratio equal to unity.

This modified version of Thomason's criterion is best suited for materials with initial porosities less than 1 % and has been applied to steel and aluminum alloys (Chen and Lambert 2003; Zhang et al. 2000). Another successful variant of the plastic limit-load model was proposed by Ragab (2004a) and has been applied to many materials by Ragab (2004a). This variant was found to predict fracture strains in much better agreement with the experimental fracture strains than other variants of the Thomason (1990) model. For spherical voids, plastic constraint factor in the Ragab (2004b) coalescence model is:

$$C_{f-R} = \left(1 + \frac{2}{\chi^{-1} - 1}\right) \ln\left[1 + \frac{1}{2}(\chi^{-1} - 1)\right] \left(\frac{\varepsilon_{\text{lig}}}{\varepsilon_{\text{uc}}}\right)^{\text{n}} \tag{2.27}$$

where ε_{lig} is the ligament strain; ε_{uc} is the average effective strain in the unit cell; The strain in the ligament can be related to the geometry of unit cell for spherical voids and small void volume fractions as

$$\varepsilon_{\text{lig}} = 2 \ln\left[\left(\frac{1 - \chi^{-1}}{1 - \chi_{\text{o}}^{-1}}\right)\left(\frac{f}{f_{\text{o}}}\right)^{\frac{1}{3}}\right] \tag{2.28}$$

and the average macroscopic strain for the unit cell is taken as $\varepsilon_{\text{uc}} = \varepsilon_1$ (Ragab 2004b). The adoption of the ligament strain hardening term in Eq. (2.27) improves the physical foundation of the model since the strain in the intervoid ligament increases faster than the bulk strain in a unit cell. However, most engineering materials do not infinitely harden and in the author's numerical experience, coalescence does not generally occur until later in deformation when the flow stress has all but saturated. Consequently, the ligament hardening term in Eq. (2.27) can be omitted in materials that possess a flow stress response that saturates at higher plastic strains. Additionally, complications arise if void nucleation is considered because the initial geometry used in Eq. (2.28) is no longer valid.

2.7.2.3 Post-coalescence Treatment When Using a Plastic Limit-Load Coalescence Model

The post-coalescence model of Tvergaard and Needleman (1984) in Eq. (2.24) is retained when using a plastic limit-load coalescence model by identifying the porosity when the coalescence condition is satisfied as the critical porosity, $f_{\text{c}} = f$. The fracture porosity can also be removed as a material parameter by re-working the physically-sound post-coalescence model of Scheyvaerts et al. (2010) as presented in Eq. (1.19). For the Gurson-Tvergaard model where the void is spherical at coalescence and the initial aspect ratio of the unit cell is unity, the fracture porosity in a specific unit cell geometry is

$$f_f = \begin{cases} 4f_c/\chi_c & \chi_c \geq \frac{1}{2} \\ \left(\chi_c + \dfrac{1-2\chi_c^2}{(9/2-\chi_c^2)}\right)\frac{f_c}{\chi_c^3} & \chi_c < \frac{1}{2} \end{cases} \qquad \chi_c = \left(\frac{f_c}{\gamma_{\text{cell}}} e^{\frac{3}{2}\left(\varepsilon_1 - \varepsilon_{\text{hyd}}\right)_c}\right)^{1/3} \quad (2.29a, b)$$

where $\left(\varepsilon_1 - \varepsilon_{\text{hyd}}\right)_c$ is the principal deviatoric strain when the critical porosity is reached. Equation (2.29) can also be used to estimate the failure porosity when using the critical porosity coalescence model. Note that Eq. (2.29) is approximate since the void shape and the initial aspect ratio are not considered, introducing error into the computation of the spacing ratio, χ, which tends to be overestimated. For example, from unit cell simulations of an axisymmetric unit cell containing an initially spherical void at a stress triaxiality of unity and a hardening exponent of 0.10, $f_c = 6.17\ \%$ at a strain of 0.46. The void aspect ratio at coalescence is 1.56 and the actual spacing ratio is $\chi \sim 0.49$. By assuming the void remains spherical, the spacing ratio is is $\chi \sim 0.57$ and this will result in a larger predicted porosity at failure in Eq. (2.29). This overestimation generally increases with decreasing stress triaxiality since the void shape will not be spherical at coalescence. Fortunately, the porosity at failure is not a critical parameter and this will not have an overly deleterious influence on the fracture strains in a finite-element simulation of a metal forming operation.

The above modifications to the GTN framework dramatically improve the predictive capabilities of the model by removing two material parameters, f_c and f_f, and computing them using physically-sound models that predict coalescence and fracture as a consequence of the evolution of the stress state and the microstructure. Only the parameters related to the nucleation model remain to be identified, paving the way for the identification of unique-nucleation parameters that are transferrable to different stress states and this will be addressed in Chap. 4.

2.8 Lower Bound Solution of Sun and Wang

Following the success of the Gurson-Tvergaard constitutive model, Sun and Wang (1989) derived the analogous lower bound solution using the spherical unit cell geometry of Gurson to obtain a conservative estimate for the yield stress and formability. While Gurson applied a velocity field to the surface of the spherical unit cell, Sun and Wang (SW) applied a prescribed traction to obtain the lower bound solution. Similar to the original Gurson formulation, Sun and Wang's yield criterion does not account for void coalescence in a meaningful way and requires large porosities before the load carrying capacity is lost. Fortunately, the same treatments of void coalescence described previously for the Gurson model can also be applied to the SW model. The Sun and Wang yield criterion is expressed as

$$\Phi = \frac{\Sigma_{\text{eq}}^2}{\bar{\sigma}^2} + \frac{b_1 f \cosh\left(\frac{3}{2}\frac{\Sigma_{\text{hyd}}}{\bar{\sigma}}\right)}{\sqrt{1 + b_3 f \sinh^2\left(\frac{3}{2}\frac{\Sigma_{\text{hyd}}}{\bar{\sigma}}\right)}} - b_2 = 0 \qquad (2.30)$$

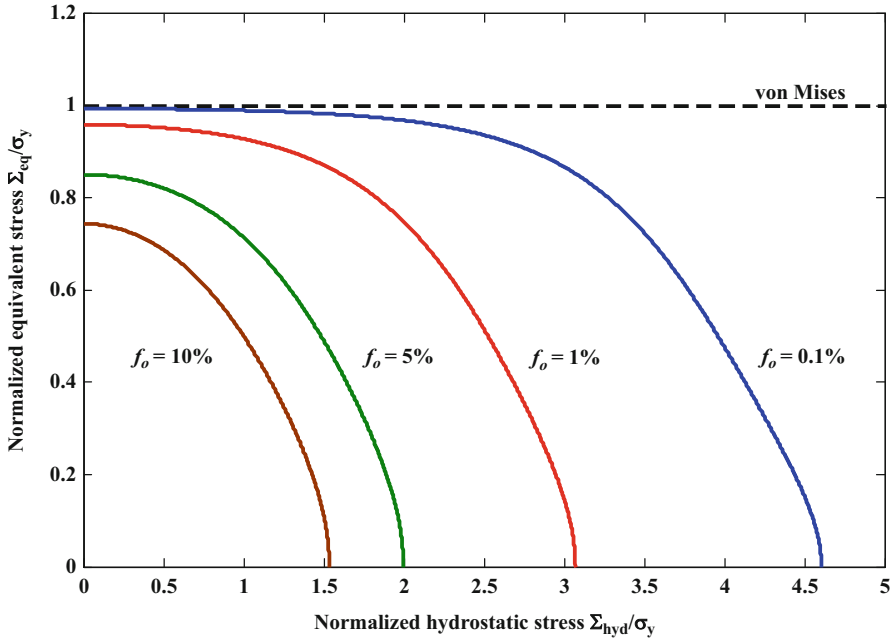

Fig. 2.10 Variation of the Sun and Wang (1989) yield surface with the hydrostatic stress and porosity

where

$$b_1 = 2 - \frac{1}{2}\ln f \qquad b_2 = 1 + f(1 + \ln f)$$

$$b_3 = \left(\frac{b_1}{b_2}\right)^2 \coth^2\left(\frac{3\Sigma_{mt}^0}{2\bar{\sigma}}\right) - \left(f^2 \sinh^2\left(\frac{3\Sigma_{mt}^0}{2\bar{\sigma}}\right)\right)^{-1}$$

$$\Sigma_{mt}^0 = -0.65\ln(f)\bar{\sigma}$$

Sun and Wang's model converts to Gurson's upper bound solution for spherical voids when

$$b_1 = 2 \quad b_2 = 1 + f^2 \quad b_3 = 0$$

and to the von Mises yield criterion when $f = 0$. The variation of the SW yield surface with the hydrostatic stress and porosity is presented in Fig. 2.10.

2.8.1 Void Growth, Nucleation and Coalescence

The same void growth, nucleation and coalescence rules discussed previously for the Gurson model are also applicable for the Sun-Wang model. It is important to

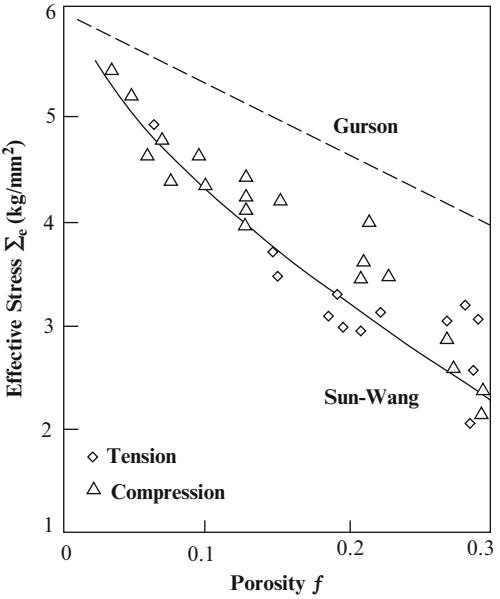

Fig. 2.11 Comparison of the *upper* and *lower* bound criteria with experimental results of Shima and Oyane (1976) for powder metallurgical materials (Reprinted with permission from Sun and Wang 1989. Copyright 1989 Springer)

note that the resulting void growth and coalescence predictions will be different than in the Gurson model due to the softer nature of the SW model which will promote higher plastic strains and thus larger void growth rates and additional material softening.

In a comparison of the upper and lower bound yield criteria with the experimental results of Shima and Oyane (1976), Sun and Wang (1989) observed yielding closer to the lower bound solution as shown in Fig. 2.11. Shima and Oyane (1976) used powder metallurgical samples to achieve porosities as high as 30 %. For a typical ductile metal, initial porosity ranges between 0.01 and 1 % (Pardoen and Hutchinson 2000). An additional work by Sun and Wang (1995) observed that the experimental porosities in sintered iron and titanium alloys were in very good agreement with the SW solution and well defined between the bounds of the SW and Gurson models as shown in Fig. 2.12. The good experimental agreement with the SW solution may be due to void distribution effects since voids that are arranged in heterogeneous clusters experience faster void growth and yielding at lower stresses and the SW model better represents that effect. Francescato et al. (2004) performed a numerical limit analysis of plasticity to compare the models of Gurson (1977), Tvergaard (1981), Richmond and Smelser (1985) and a modified form of Sun and Wang (1989) for cylindrical voids. This study observed that Sun and Wang's (1989) lower bound model closely approximates the actual solution for low porosities ($f < 5$ %) while the Richmond and Smelser (1985) model worked better for high porosities ($f > 5$ %).

The principal take-away from these figures and results is not that the SW model is superior to the Gurson model since there are surely cases where the experiment is

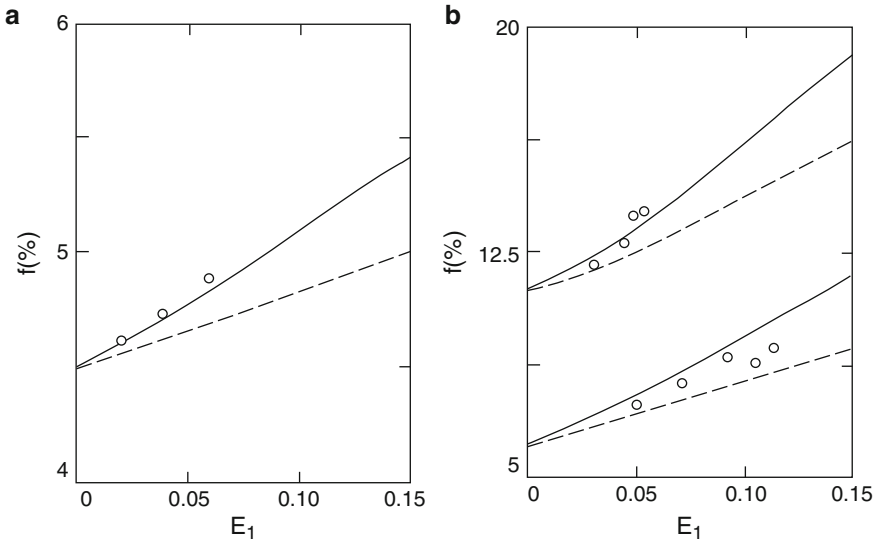

Fig. 2.12 Increase of the void volume fraction, f, as a function of the uniaxial strain: (**a**) experimental data for a Sintered CP Ti alloy from Marciniak and Kuczynski (1967). (**b**) Experimental data for Sintered iron by Bourcier et al. (1986). The solid line denotes the SW model and the dotted-line denotes the prediction of the Gurson (1977) model. Note that the SW model provides the upper limit for the porosity since it is softer than the Gurson model (Reprinted with permission from Sun and Wang (1995). Copyright 1995 Springer)

better described by the Gurson model, but rather that neither of these models is overly accurate. Only by utilizing both upper and lower bound solutions can the material behaviour be well represented in a meaningful way since these are approximate yield criterion with highly idealized void distributions.

2.9 Upper and Lower Bound Approach to Ductile Fracture of Porous Materials

The Gurson model has received significant attention since its introduction while the lower bound Sun-Wang model has gone largely unnoticed. An exhaustive number of Gurson-based models have since been developed to account for many different effects such as void shape (Pardoen and Hutchinson 2000; Ragab 2004a; Wen et al. 2005; Lassance et al. 2006), non-local damage development (Tvergaard and Needleman 1995; Leblond et al. 1994; Reusch et al. 2003), and anisotropic materials (Liao et al. 1997; Chein et al. 2001; Wang et al. 2004; Kelavelarma and

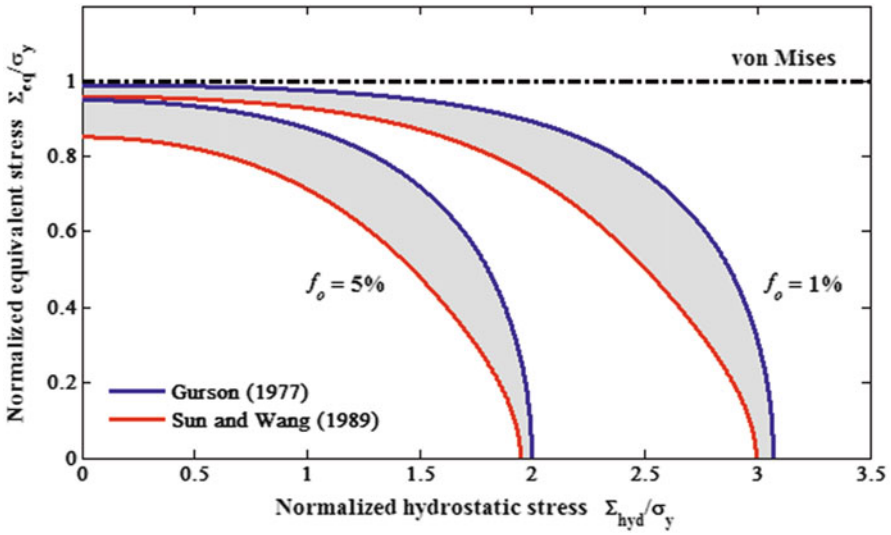

Fig. 2.13 Yield surfaces of the von Mises, Gurson (1977) and Sun and Wang (1989) models. The experimental yielding behaviour of a material should lie on or between the two bounds within the shaded band. The macroscopic equivalent and hydrostatic stress are normalized by the yield stress of the material (Reprinted with permission from Griffin et al. (2011). Copyright: Springer)

Benzerga 2009; Cazacu and Stewart 2009). Nowadays, the GLD (Gologanu, Devaux and Leblond) model (Gologanu et al. 1997) has largely replaced the GT model and its variants in the academic community due to its natural ease in describing the void shape effects that are critical to the accurate modeling of void coalescence. Unfortunatley, Sun and Wang's lower bound solution has only been modified to include kinematic hardening (Yan 1992), shear localization (Sun and Wang 1995; Sun 1995a) and a dual population of large and small voids (Sun 1995b). A lower bound solution to the ellipsoidal unit cell geometry of Golaganu et al. (1997) would provide an excellent counterpoint to the GLD model and enable the prediction of upper and lower forming limits using advanced void coalescence models.

The use of both upper and lower bound damage models can provide a novel and straightforward method to obtain estimates of the formability of ductile materials by acknowledging the inherent limitations of the models and exploiting the difference in the yield surfaces as shown in Fig. 2.14. The shaded band in Fig. 2.13 can be interpreted as the formability band for the actual yield stress of a material and it is expected to fall within this range. By employing the same void nucleation and coalescence models in both the upper and lower bound yield criteria, a range for the limiting strains or formability band for the material can be defined.

An important distinction in this approach is that although one of the yield criteria may be more accurate in an academic sense in that it matches the the numerical bound obtained from FE simulations of a spherical unit cell for a given stress state, this is of secondary importance because real materials do not adhere to such a rigid

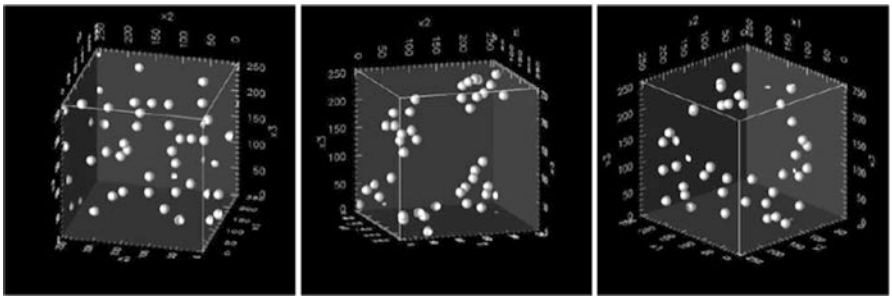

Fig. 2.14 Three-dimensional clustered microstructures of Bilger et al. (2005): random (*left*), disconnected clusters (*center*) and connected clusters (*right*) (Reprinted with permission from Bilger et al. (2005). Copyright 2005 Elsevier)

definition of the microstructure. The actual material behaviour will generally fall within the two bounds due to void distribution effects and other factors that are not considered in the models such as shearing, particle-void interactions, etc. It is important to not interpret the predicted upper and lower forming limits defined by the GT and SW models in an absolute mathematical sense because they are approximations to the microstructure and spherical unit cells do not strictly adhere to the definition of a periodic microstructure. Consequently, it is possible for the experiment behaviour to lie outside of these bounds but together they generally provide very good estimates. The upper and lower bound approach accepts that these models are inherently approximate and that there is value in estimating the material behaviour within a range. The following sections will discuss the evolution of the dual-bound approach to ductile fracture developed by the authors and its application to a variety of metal forming operations.

2.9.1 Application of the Dual Bound Approach to Porous Materials with Void Clusters

Inherent in the upper and lower bound formulations of Gurson (1977) and Sun and Wang (1989) is the assumption that the voids remain spherical and the material can be composed of a periodic assembly of spherical unit cells. However, real materials often contain a dilute concentration of voids that are heterogeneously distributed in clusters and the periodic assumption becomes a necessary yet questionable assumption in order to obtain a tractable geometry to derive the yield criteria. In this instance, it is important to evaluate the performance of the damage-based yield criteria as neither is expected to perform overly well in this situation. The work of Bilger et al. (2005) provides an interesting opportunity to evaluate this condition since they considered the overall and local responses of porous media composed of a perfectly plastic matrix with spherical voids in various arrangements. Bilger et al. (2005) employed the Fast Fourier transform (FFT) method to numerically

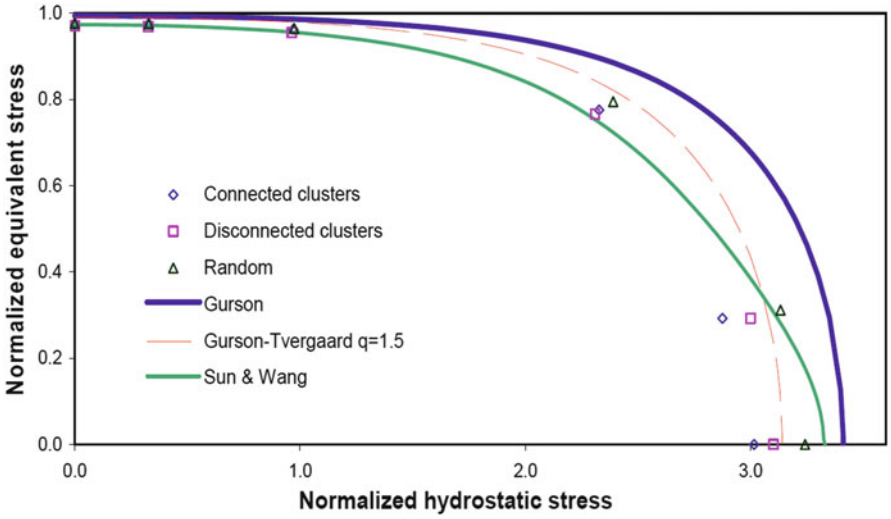

Fig. 2.15 The Gurson and SW yield surfaces have been superimposed onto the numerical results of Bilger et al. (2005) for type-A loading (pure shear with hydrostatic tension) (Reprinted with permission from Griffin et al. (2011). Copyright: Springer)

determine the onset of yielding in materials having microstructures characterized by one of three void spatial distributions:

i. a random void distribution without void clustering,
ii. connected clusters of voids, or
iii. disconnected clusters of voids.

The study considered two-dimensional and three-dimensional arrangements, each under two loading types (type-A, that combined pure shear with a superimposed hydrostatic tension, and type-B which did not have a shear component) over a large range of stress triaxiality. Only the three-dimensional arrangements are considered here because there is no analogous 2-D lower bound solution of the Sun-Wang model. The total void volume fraction in the microstructures is 0.6 % and the various cluster arrangements are presented in Fig. 2.14.

Bilger et al. (2005) compared their results with the Gurson-Tvergaard (GT) model which proved to be overly stiff and overestimated yielding in the different microstructures. Griffin, Butcher and Chen (2011) noticed the overestimation of the GT model and evaluated the lower bound criterion of Sun and Wang (1989) using the results of Bilger et al. (2005). The SW model is inherently more sensitive to the porosity than the Gurson model and experiences earlier yielding and additional material softening. The lower bound solution of SW was superimposed on the results of Bilger et al. (2005) as shown in Figs. 2.15, 2.16 and 2.17 to evaluate the performance of the dual bound approach first applied in Butcher et al. (2006). For clarity, Fig. 2.18 shows a close-up view of the results at low stress triaxialities. To provide a contrast with the traditional Gurson model, the more-commonly employed GT solution with fitting parameter $q = 1.5$ is shown for comparison with the original Gurson and SW models.

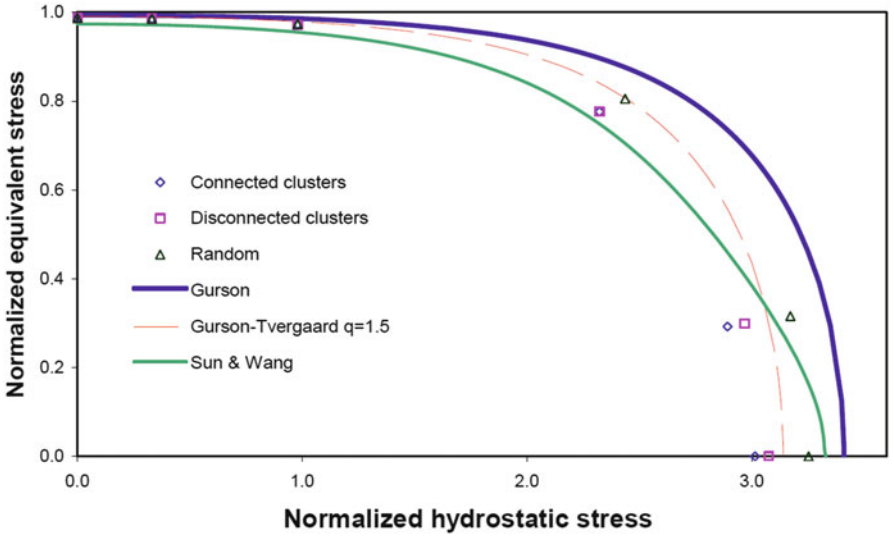

Fig. 2.16 The Gurson and SW yield surfaces have been superimposed on the numerical results of Bilger et al. (2005) for type-B loading (hydrostatic tension, no shear) (Reprinted with permission from Griffin et al. (2011). Copyright: Springer)

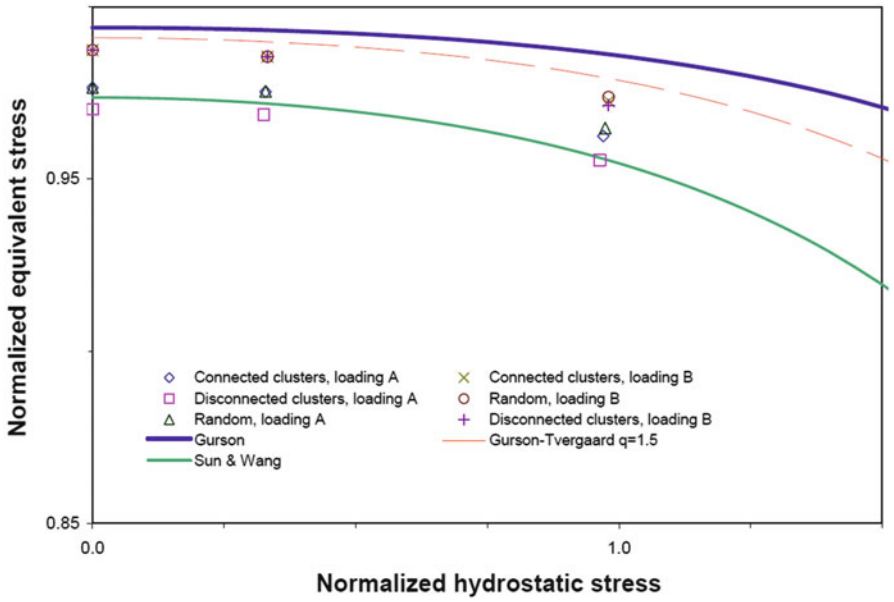

Fig. 2.17 Comparison of the three-dimensional macroscopic yield surfaces with the numerical results of Bilger et al. (2005) for two different loading conditions at low triaxialities (Reprinted with permission from Griffin et al. (2011). Copyright: Springer)

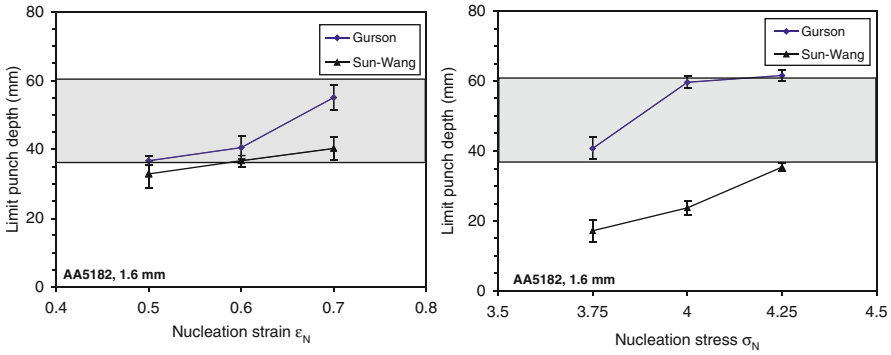

Fig. 2.18 Limit punch depth versus void nucleation strain (*left*) and stress (*right*) for AA5182 1.6 mm sheet; the *shaded band* represents the experimental results for failure due to circumferential cracking (Reprinted with permission from Butcher et al. (2006). Copyright: Springer)

For low stress triaxialities the results are well captured within the upper and lower bound predictions which is fortuitous since the practical range of stress triaxiality is less than unity for a sheet metal forming operation. Notice that none of the yield criteria were able to give great results for all of the stress states and microstructures considered. Despite the different loading conditions, stress triaxialities and microstructures, the dual bound approach is able to provide very good upper and lower estimates for the yield behaviour.

This is a significant advantage of the dual bound approach because although neither model was derived for void clusters or shear loading, a good representation of the material behaviour can still be captured between the two bounds. By obtaining upper and lower estimates for the material behaviour, the variation in the material behaviour due to deviations from the assumption of a periodic void distribution can be better captured than if using a single model. From a practical perspective, it is reasonable to expect the material response to usually fall within the upper and lower limits as predicted by the approximate models of Gurson and Sun and Wang. This result is very attractive to industry because the original Gurson and Sun and Wang models can be quickly implemented in a commercial finite-element code and employed to obtain a first-order prediction of the material behaviour in a forming process of interest.

2.10 Application of the Dual Bound Approach to a Stretch Flange Forming Process

The first application of the dual bound concept was performed by Butcher et al. (2006) for a stretch flange forming operation of AA5182 sheet. One example of a stretch flanging operation is to expand a cutout in a blank to create the openings for

Table 2.1 Controlling parameters in GTN-based and Sun and Wang material models

Model	q_1	q_2	q_3	f_o	f_c	f_f	f_u	f_n	s_n ($\% \varepsilon_N, \sigma_N$)
GTN	1.25	0.95	1.5625	0	0.01	0.02	0.80	0.00768	20
Sun-Wang	–	–	–	0	0.01	0.02	0.80	0.00768	20

windows in car door panels. Details of the stretch flange forming process, experiments and finite-element modeling will be discussed in detail in Chap. 6. The lower bound SW model was implemented along with the GT model into LS-DYNA (Hallquist 2006), a commerical finite-element solver, using user-defined subroutines. Void nucleation was assumed to be either stress- or strain-controlled using the nucleation models of Chu and Needlemen (1980) described in Eq. (1.5). The rather simplistic critical porosity coalescence model of Tvergaard and Needleman (1984) was used since a detailed metallographic and numerical analysis of the material was performed by Chen (2004) and an appropriate critical porosity was identified. The controlling parameters used in the simulations are presented in Table 2.1. A minor limitation in this study was that the q_i parameters were not set to unity so that the formal upper bound of Gurson (1977) was slightly artificially softened by using the suggested q_i values of Koplik and Needleman (1988).

2.10.1 Predicting the Limit Punch Depth

Cutout sizes ranging from 88 to 98 mm were considered and the effect of the cutout size on the limiting punch depth was small. No correlation was observed between the onset of a radial crack at the cutout edge or the formation of a circumferential crack. The FE model was only able to predict the onset of a circumferential crack because the model was axisymmetric. Consequently, the experimental limit punch depths for the circumferential cracks for all of the cutout sizes are presented as a single shaded band in Fig. 2.18 (Chen 2004). The nucleation stress and strain were then parametrically identified in the SW and GT models until the predicted formablity band matched the experimental band for the limit punch depth. It was observed that a nucleation strain of 0.70 and a nucleation stress of $4.25\sigma_y$ (~500 MPa) gave good results.

2.10.2 Damage Evolution During Forming

Damage evolution is expressed as a function of punch displacement in the element of interest (EOI) and the punch displacement is measured relative to the main punch. The backup punch moves upwards to close the drawbead and stretching begins as the main punch moves downward as described in Chap. 6. To clearly

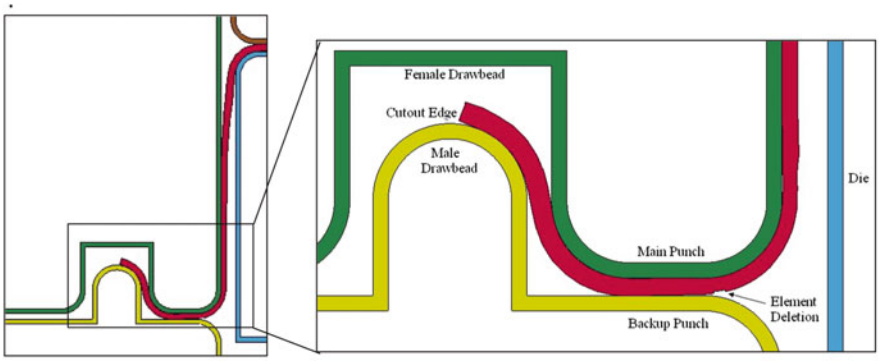

Fig. 2.19 Element deletion due to void coalescence at limit punch depth (Reprinted with permission from Butcher et al. (2006). Copyright: Springer)

present damage evolution as a function of punch displacement, the change in direction of the punches is neglected and drawbead closure corresponds to a displacement of 0 mm. Damage development is typically negligible until the blank leaves the drawbead and enters the punch profile. Upon entering the punch profile, void growth and nucleation occur resulting in the formation of a circumferential crack in the side-wall of the flange or at the punch nose as shown in Fig. 2.19. In the simulation, this coincides with the onset of element deletion, forcing the porosity measurement to zero and the termination of the simulation. The limit punch depth is then extracted. The element initially in contact with the male drawbead typically exhibits the highest damage rate during stretch-flange forming. Therefore, it is chosen as the element of interest (EOI) to characterize damage evolution.

2.10.3 Comparison of the Predicted and Measured Porosity

To validate the predicted damage evolution in the element of interest, the porosity history obtained using the strain and stress-based nucleation rules are compared with the damage measurements of Chen (2004) in Figs. 2.20 and 2.21, respectively. To experimentally measure damage evolution in the element of interest, Chen (2004) performed a series of interrupted tests to obtain damage measurements as a function of punch displacement. In each test, the area of interest which was sectioned and the through-thickness porosity measured using standard thresholding techniques.

It is important to note that the porosity measurements of Chen (2004) are not definitive due to the digital imaging process. To measure porosity, the sample is digitally scanned with a high resolution digital camera. From these images, the background can be eroded to leave the voids which will be darker than the background. This process can be very sensitive to the parameters used in the imaging process and small variations in the parameters may lead to different porosity measurements. This sensitivity is further compounded by the small damage level required to cause fracture in the 5xxx series alloys. With this in mind, the porosity

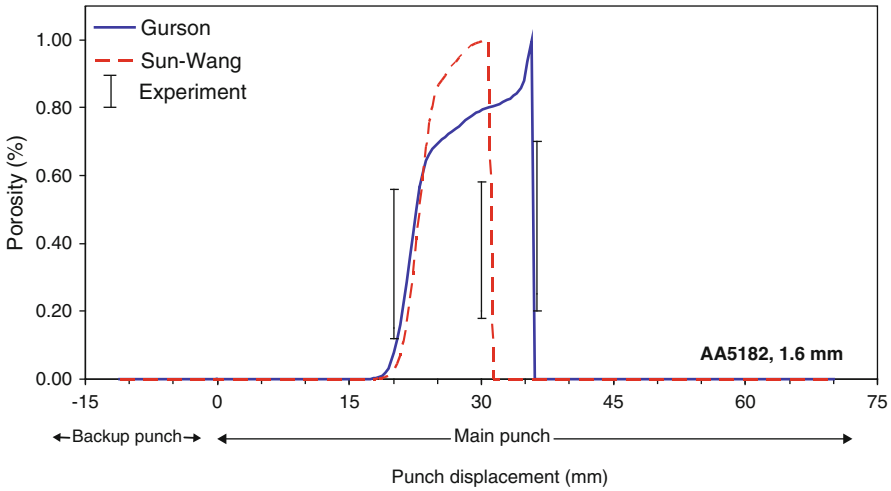

Fig. 2.20 Comparison of experimental and predicted damage evolution in the EOI for an 88 mm cutout and nucleation strain of 0.5

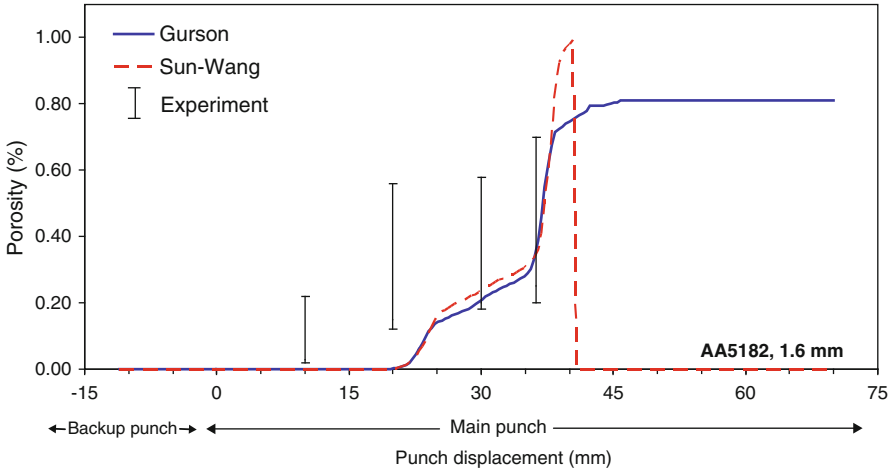

Fig. 2.21 Comparison of experimental and predicted damage evolution in the EOI for an 88 mm cutout and nucleation strain of 0.7

results are presented to provide a guideline of actual damage evolution in the stretch flange forming.

For strain-controlled nucleation, Figs. 2.20 and 2.21 demonstrates that porosity is not accurately predicted as both upper and lower bound models predict marginal damage development until a punch depth greater than 15 mm. However, the Gurson model gives a reasonable prediction of porosity for a nucleation strain of 0.5 while both models significantly underestimate damage for a strain of 0.7.

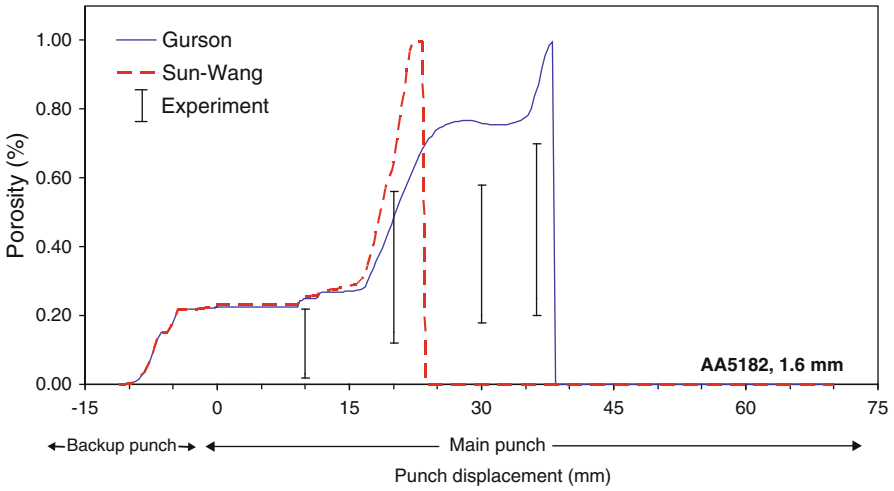

Fig. 2.22 Comparison of experimental and predicted damage evolution in the EOI for an 88 mm cutout and nucleation stress of $3.75\sigma_Y$

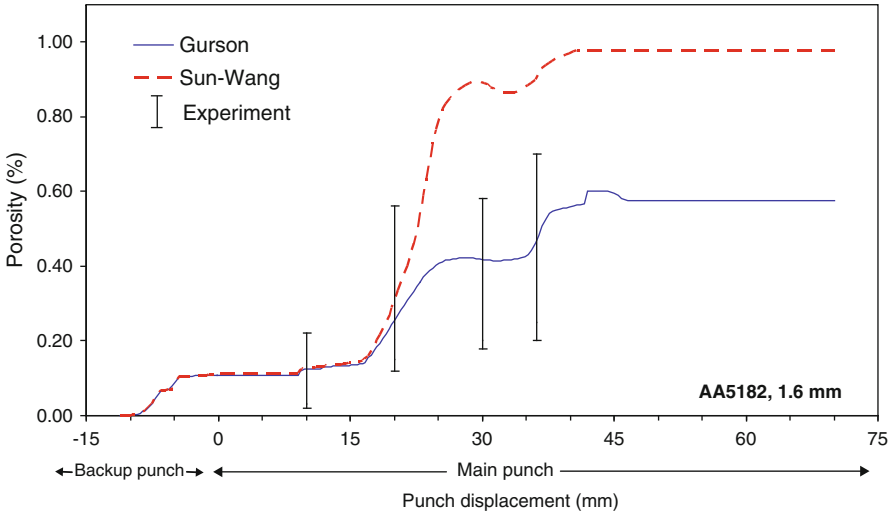

Fig. 2.23 Comparison of experimental and predicted damage evolution in the EOI for an 88 mm cutout and nucleation stress of $4.25\sigma_Y$

Damage evolution for the stress-based nucleation model clearly gives much better agreement with the experiment as demonstrated in Figs. 2.22 and 2.23. Both upper and lower bound models capture the experimentally measured porosity with the Gurson model giving a better prediction since the lower bound model fails prematurely at this nucleation strain. For a nucleation strain of $4.25\sigma_y$ (Fig. 2.24), both upper and lower bound models give very good agreement with the experiment.

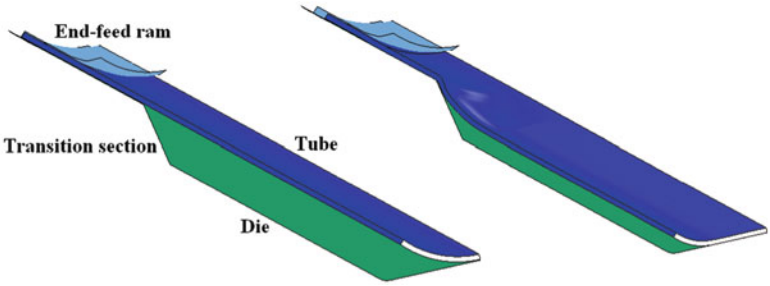

Fig. 2.24 One-eighth finite-element model of the initial tube (*left*) and formed tube (*right*) (Reprinted with permission from Butcher et al. (2009). Copyright: Springer)

The lower bound model provides an upper limit on porosity with the Gurson model giving a lower limit. Despite the scatter in the porosity measurements, stress-based nucleation gives realistic damage predictions in both models.

2.11 Application of the Dual Bound Approach to Ductile Fracture in Tube Hydroforming

Tube hydroforming is attractive to the automotive industry since it can produce low weight, high strength and uniform parts while eliminating traditional welding and stamping operations. A typical hydroforming operation involves pressurizing the inside of a tube to conform to the cross-section of a die. The hydroforming of advanced high strength steels (AHSS) such as DP600 offers benefits such as a more continuous yielding behaviour, higher work hardening limit and total elongation-to-failure compared to traditional high-strength low alloy steels (HSLA). Despite the apparent advantages of hydroformed AHSS components, formability is limited due to the initiation of microvoids (damage) that grow and coalesce leading to sudden fracture.

While void damage has typically been neglected in hydroforming simulations, Baradari (2006), Varma et al. (2007) and Butcher et al. (2009) have shown that good predictions of formability can be obtained using Gurson-based constitutive models. A previous study by the authors (Butcher et al. 2009) applied an advanced Gurson-based constitutive model to the hydroforming of DP600 steel that accounted for void shape effects, stress- and strain-based nucleation and coalescence due to both internal necking and shearing. While this model has shown some success in predicting formability, a large number of material parameters were required to describe each stage of damage evolution. The subsequent identification of these parameters can be prohibitive to the adoption of these models by industry. The dual bound approach provides a straightforward solution to this problem by focusing on using simpler damage-evolution rules and exploiting the upper and lower bound nature of the models. Instead of expecting a complicated single-bound

model to provide an absolute prediction of ductility, the focus is to capture the behaviour within a band. In this manner, it is not essential that a single-bound completely describe the material behaviour just that the formability lies within the limits defined by both models.

The dual bound approach was applied to the straight-tube hydroforming model of Butcher et al. (2009) for DP600 steel tubes to determine the burst pressure, formability and failure location. Compressive axial loads of 0 and 133 kN were applied to the tube during forming to evaluate performance of the models in different loading conditions. A simple strain-controlled void nucleation rule was adopted for both damage models and calibrated to provide forming limits that capture the experiment data. Finally, the performance of the calibrated dual-bound models is compared with the formability predictions of Butcher et al. (2009) who used an advanced variant of the Gurson (1977) model.

2.11.1 Constitutive Modeling

The dual constitutive models are the same as used in the previous section with the exception that the q_{i} parameters in the GT model are set to unity to recover the upper bound solution of Gurson (1977) and that void nucleation is strain-controlled. The continuous nucleation model of Gurland (1972) was adopted where the nucleation rate is proportional to the plastic strain rate

$$\dot{f}_{nucleation} = A_N \dot{\varepsilon}^{\mathrm{p}} \tag{2.31}$$

where A_N is the nucleation intensity and $\dot{\varepsilon}^{\mathrm{p}}$ is the plastic strain rate. The continuous nucleation model only requires one parameter, A_N, to be identified from experiment compared to three parameters in the well-known Chu and Needleman (1980) model. Zhang and Niemi (1994a) demonstrated that the simpler continuous nucleation model can perform equally as well as the Chu and Needleman model (1980) where the nucleation intensity is assumed to follow a normal distribution. The authors have also observed that the continuous strain nucleation model can provide nearly equivalent predictions to the more complicated Chu and Needleman (1980) in some unpublished numerical studies.

2.11.2 Material Characterization

2.11.2.1 Material Properties

Tensile samples were obtained from the tubes at orientations of 3, 6 and 9 o'clock relative to the weld seam and averaged to determine the flow stress-strain relation (Bardelcik 2006). Although the stress state in hydroforming is biaxial stretching,

Table 2.2 Mechanical properties of DP600 steel tubes reported by Bardelcik (2006)

Material	E (GPa)	v	σ_y (MPa)	K (MPa)	n
DP600	206	0.30	413.54	795.8	0.115

Table 2.3 Controlling parameters in the material models

f_o	f_c (%)	f_f (%)	A_N
0	0.7	2	Identified parametrically

using the uniaxial flow stress relation is reasonable for DP600 since the forming limit curve (FLC) determined using sheet specimens gives very good agreement with the FLC determined using hydroformed tubes (Asnafi and Skogsgardh 2000). The averaged flow stress curve was converted to a plastic strain-true stress curve in the form of $\bar{\sigma} = K\varepsilon^n$ and linearly extrapolated from approximately 0.15 strain (ultimate tensile strength point) to 0.60. The tube stock had an average thickness of 1.85 mm with an outer diameter of 76.2 mm. The mechanical properties of DP600 are presented in Table 2.2.

2.11.2.2 Selection of Damage-Based Material Parameters

The DP600 steel tubes are composed of 5.5 % martensite in a banded-type formation and is considered to be initially damage-free with an initial porosity, f_o, of zero (Winkler et al. 2008). Uniaxial tensile tests were conducted by Winkler et al. (2008) using the same tube material used in the hydroforming experiments. 2-D metallographic analysis revealed the porosity (area fraction) near the fracture surface to be about 0.7 % and this value is taken as the critical porosity. The porosity at fracture is assumed to be 2 % (Maire et al. 2008). The only parameter required to be identified is the nucleation intensity, A_N, which is determined parametrically by comparing the numerical formability predictions of both damage models to the hydroforming test data. The value of A_N is selected that yields the best agreement with the experimental forming limits for both end-feed loads. The controlling parameters used in the damage-based constitutive models are shown in Table 2.3. Note the few parameters that exist in the model with the major parameters being the critical porosity and the nucleation intensity. If the plastic-limit load coalescence model was used then the critical porosity term can be removed from the analysis (Butcher et al. 2009). The initial porosity can safely be set to zero or a small value for a clean material such as DP600 and the porosity at fracture has minimal impact on the solution.

2.11.3 Finite-Element Model

The tube was modeled with 80,000 eight-node constant stress brick elements and the surfaces of the steel die and end-feed rams are rigid and meshed using

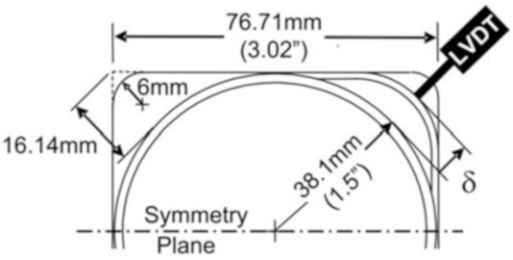

Fig. 2.25 Section of the hydroforming die showing corner-fill expansion (Reprinted with permission from Bardelcik (2006). Copyright 2006 Bardelcik)

quadrilateral shell elements. Contact between the tube, die and rams is modeled using a penalty-based contact algorithm available in LS-DYNA (Hallquist 2006). The coefficients of friction (COF) between the tube and die and tube and rams were experimentally determined using a twist-compression test as 0.035 and 0.08, respectively (Bardelcik 2006).

A null shell mesh coincident with the solid mesh of the tube is used to apply the pressure load. The tube is pre-pressurized to 35 MPa to avoid buckling before the end-feed load is applied and maintained using load control. The full EF load is applied from 35 to 38 MPa and then pressure is linearly increased to 152 MPa. For the zero end-feed case, the rams remain stationary and the end-feed load is adjusted to counteract the internal pressure on the face of the ram. The initial and formed tube models are shown in Fig. 2.24. The forming limit is detected at the onset of element deletion signifying localized necking and the onset of failure. The satisfaction of the post-coalescence criterion in Eq. (2.24) triggers element deletion in the finite-element model with widespread fracture of the tube occurring at the onset of element deletion.

2.11.4 Measuring Formability

Formability is defined using the corner-fill expansion (CFE) which measures the change in the cross-section of the tube from circular to rectangular with a CFE of 100 % corresponding to a perfect square. A section of the hydroforming die showing corner-fill expansion is presented in Fig. 2.25.

Corner-fill expansion is expressed as

$$\text{CFE } (\%) = \frac{100\delta}{\delta_{\max}} \tag{2.32}$$

The maximum corner distance between the tube and die is 16.14 mm. However, the maximum CFE achievable is 84.3 % of this distance due to the fillet corner radius as shown in Fig. 2.25. To present formability using an absolute scale, CFE in the present work is defined as

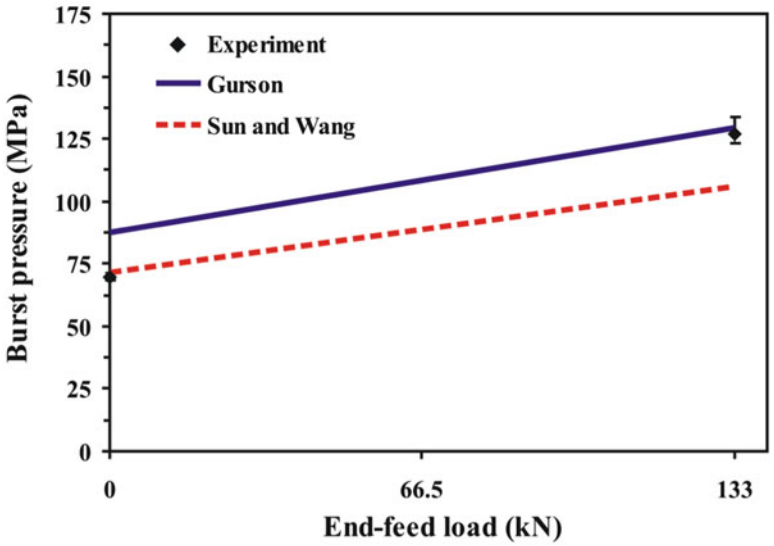

Fig. 2.26 Comparison of the experimental burst pressure with the *upper* and *lower* limits obtained using the Gurson and Sun and Wang material models for end-feed loads of zero and 133 kN. The nucleation intensity is 0.021

$$\text{CFE } (\%) = \frac{100}{0.843} \frac{\delta}{16.14 \text{ mm}} = 7.35\delta \tag{2.33}$$

Corner-fill expansion was measured at 90 % of the average burst pressure for each end-feed load and the results of Bardelcik (2006) have been restated according to Eq. (2.33). Further details related to the hydroforming experiments and development of the finite-element model can be found in Bardelcik (2006).

2.11.5 Results

A parametric study was conducted to determine the void nucleation intensity that provides good agreement with the experimental burst pressure, formability and failure location for each end-feed load and material model. A nucleation intensity of 0.021 successfully captures the experimental burst pressure and formability within the band defined by the upper and lower bound material models.

2.11.5.1 Tube Burst Pressure

The resulting band for burst pressure is compared with the experimental results in Fig. 2.26. The dual bound approach is able to capture the experimental burst

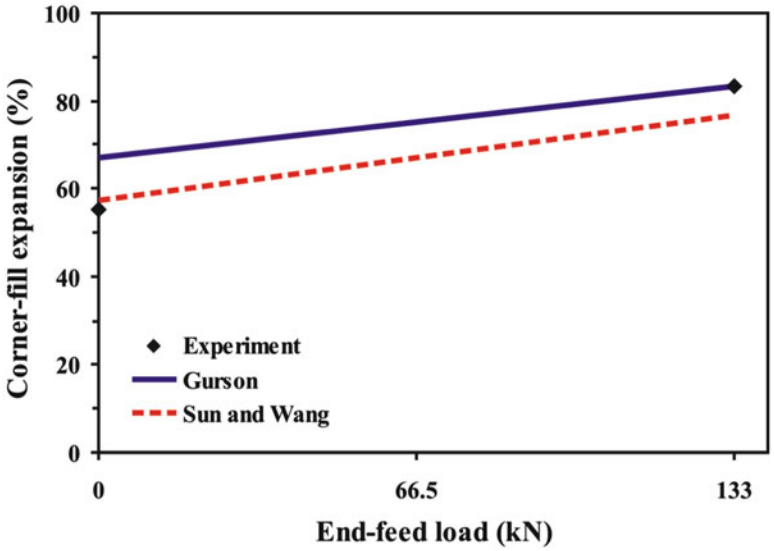

Fig. 2.27 Comparison of the experimental corner-fill expansion with the upper and lower limits obtained using the Gurson and Sun and Wang material models for end-feed loads of zero and 133 kN. The experimental and numerical corner-fill expansion is obtained at 90 % of the burst pressure. The nucleation intensity is 0.021

pressure for both end-feed loads. The lower bound model gives best agreement in the 0 kN EF case while the upper bound Gurson model performs best for the 133 kN EF load. Conversely, the Gurson and SW models over/underestimate the burst pressure for zero and 133 kN EF, respectively. It is likely that the upper bound Gurson model performs well in the high EF case as EF promotes a more uniform stress state, thus the material can be formed to higher strain levels, which better matches the upper bound approximation of the material. The addition of a compressive axial load during tube expansion reduces the stress triaxiality resulting in a lower void growth rate that is better described by the more rigid Gurson model. The dual bound approach can reliably predict fracture in both EF cases as well as define a range for the burst pressure.

2.11.5.2 Corner-Fill Expansion

The formability band for corner-fill expansion is compared with the experiment in Fig. 2.27. The experimental and numerical CFE were obtained at 90 % of the burst pressure. No standard deviation for CFE was reported as the tests showed little variation (Bardelcik 2006). Similar to the trend for burst pressure, the lower bound model is able to accurately predict the CFE for zero EF while the upper bound model obtains excellent agreement for the 133 kN EF case. Overall, the

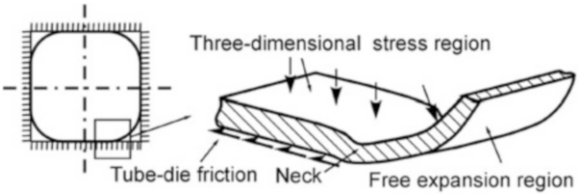

Fig. 2.28 Schematic of the stress state and localization during straight tube hydroforming (Reprinted with permission from Simha et al. (2007). Copyright 2007 ASME)

experimental results of CFE are captured within the formability band defined by the upper and lower bound models, which clearly demonstrates the advantage of the dual bound approach since CFE could not be described by a single bound model.

2.11.5.3 Failure Location

Regardless of the end-feed load, tube failure occurs in the transition region where the tube loses contact with the die and becomes free to expand (Bardelcik 2006). The material in this 'free-expansion zone' in Fig. 2.28 is under a state of plane-stress while the remaining material is under a three-dimensional state of stress. The friction between the tube and die and through-thickness compressive load due to internal pressure retard material flow into the plane-stress free-expansion zone, leading to the formation of a localized neck. The formation of a localized neck increases the local plastic strain and stress triaxiality, driving void nucleation and damage development leading to coalescence and fracture. As shown in Fig. 2.29, the application of a compressive end-feed load reduces the severity of the stress state and delays damage evolution enabling forming to higher strains.

The experimentally observed failure locations and porosity contours for 0 and 133 kN end-feed are compared with the failure location in the FE models in Figs. 2.30 and 2.31, respectively. No quantitative results for failure location were reported by Bardelcik (2006) so the comparison is qualitative. The upper and lower bound models both predict that damage becomes localized in the transition region bordering the free-expansion zone.

2.11.5.4 Void Damage

The void damage histories are presented in Fig. 2.32, which were obtained from the first element to fail for each end-feed case. The porosity histories for both upper and lower bound models exhibit a similar trend, with the softer SW model experiencing a faster rate of damage development compared to the more rigid Gurson model. End-feed effect suppresses nucleation because the compressive load forces more material into the die, reducing the effective strain and damage evolution.

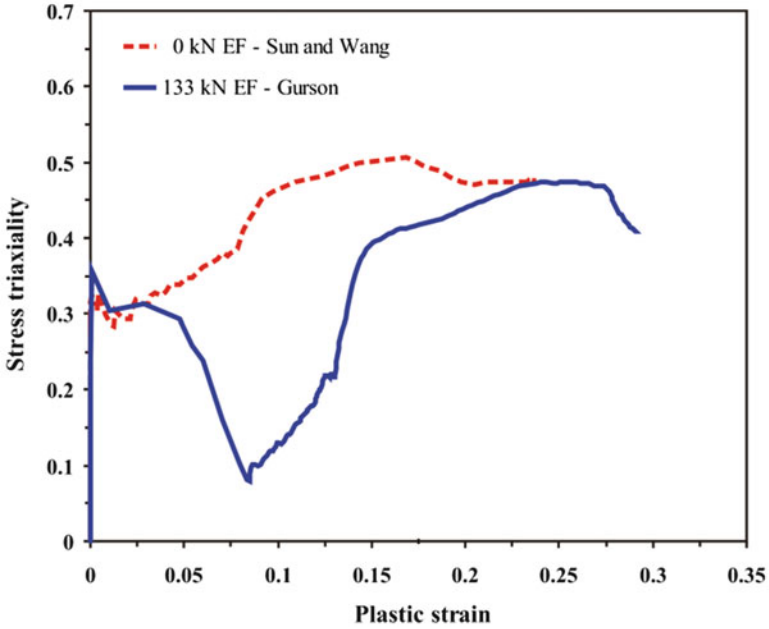

Fig. 2.29 History of stress triaxiality within the first element to fail for end-feed loads of zero and 133 kN. The stress state is obtained from the material model which gives the best performance for a particular end-feed load

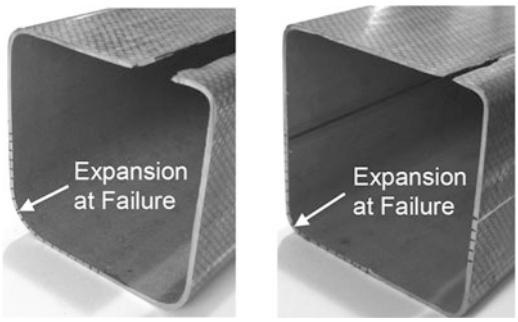

Fig. 2.30 Experimental failure locations for end-feed loads of: (**a**) 0 kN and (**b**) 133 kN (Reprinted with permission from Butcher et al. (2009). Copyright: Springer)

The dual bound approach enables a porosity band to be obtained for each loading condition which is valuable for comparison with experiment due to the variation present in porosity measurements. Experimental porosity data was not available for the fractured tubes and the porosity trends should be considered qualitative in nature. Overall, the porosity trends seem to be physically reasonable since the initial, critical and final porosities are based upon experimental observations.

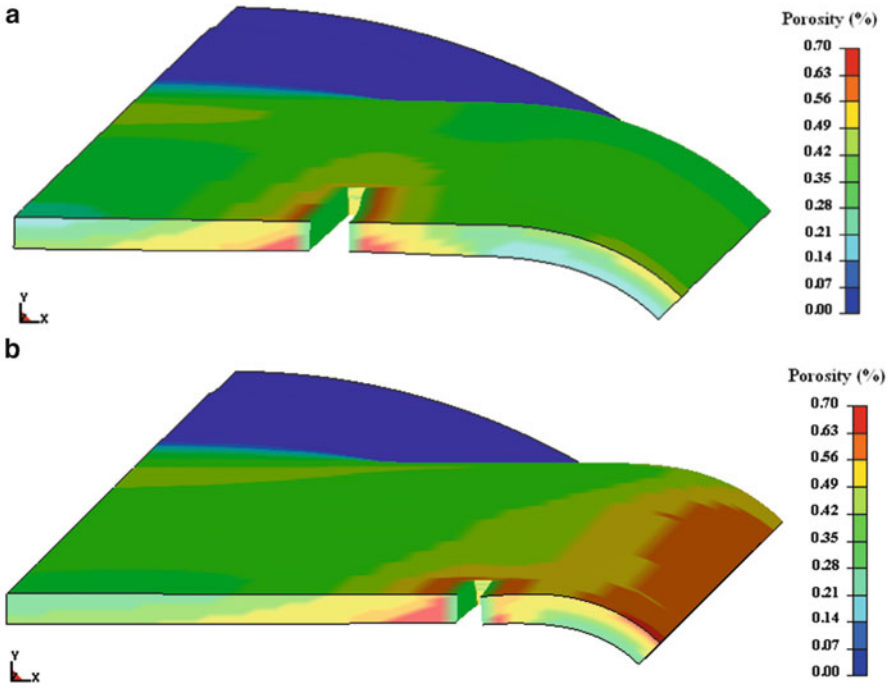

Fig. 2.31 Failure location and porosity contours for end-feed loads of (**a**) 0 kN using the Sun and Wang model and (**b**) 133 kN using the Gurson model. The failure location is obtained from the material model which gives the best performance for a particular end-feed load. One-eighth of the tube is modeled due to symmetry

2.11.6 Evaluation of the Dual Bound Approach for Tube Hydroforming

The advantages of the dual bound approach are clearly illustrated in Fig. 2.33 which compares the dual bound burst pressures to the results of Butcher et al. (2009) who employed a more sophisticated variant of the Gurson-Tvergaard-Needleman (GTN) model. This extended model accounted for the influence void shape evolution and coalescence due to internal necking and shearing of the inter-void ligaments. The stress- and strain-based nucleation models of Chu and Needleman (1980) were also considered. Despite the improved physical foundation of this model, it performed no better than the Gurson (1977) model. Only the dual bound approach could capture the burst pressure for each end-feed load.

It is important to mention that the small difference between the burst pressures obtained using the Gurson (1977) and the variant employed by Butcher et al. (2009) is coincidental because the two independently calibrated models possess different

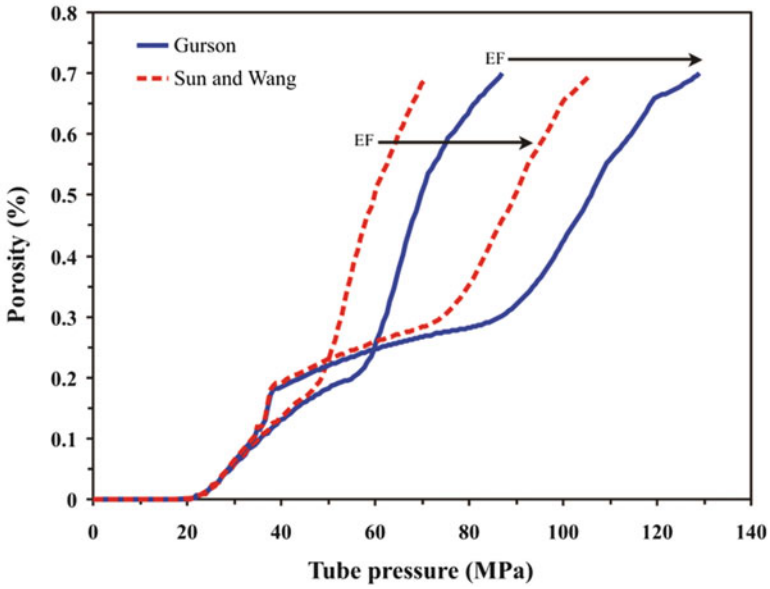

Fig. 2.32 Damage evolution within the first element to fail for end-feed loads of zero and 133 kN obtained using the Gurson and Sun and Wang constitutive models. The nucleation intensity is 0.021

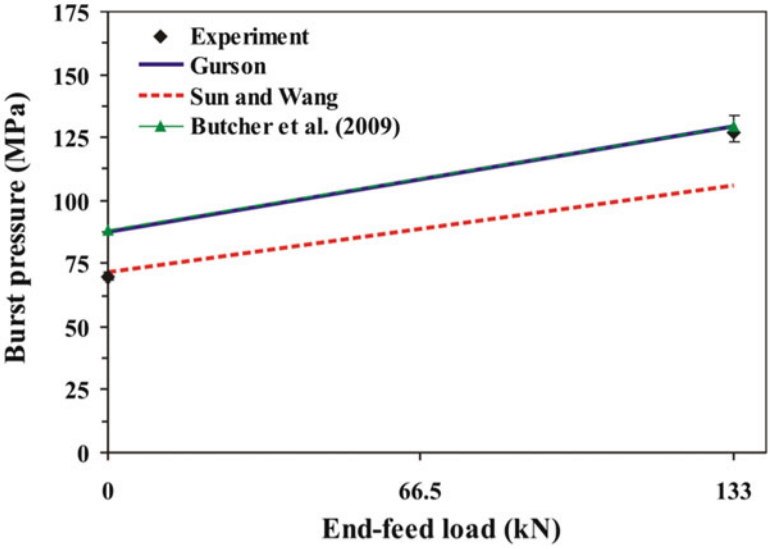

Fig. 2.33 Comparison of the experimental burst pressure with the forming limits obtained using the dual bound approach and the extended Gurson-based model of Butcher et al. (2009) for strain-controlled nucleation

models for damage evolution. Consequently, there are many combinations of models and parameters that can produce similar results. While a direct comparison is not possible, Fig. 2.33 reveals that none of the three models considered could capture the burst pressure for both end-feed loads. Only by combining the upper and lower bound models into a formability band could the burst pressure be properly described. This is a very attractive result because the dual bound approach employs simpler damage models with fewer parameters and may obtain burst pressures as good as, or better than, a single advanced model.

2.12 A Dual Bound Approach to Determining the Void Nucleation Parameters in Sheet Materials

The success of Gurson-based constitutive models in predicting ductile fracture depends on the identification of the material parameters governing void nucleation and coalescence. The void growth rule in the Gurson (1977) model does not require any material parameters since the voids are assumed to remain spherical. By adopting a coalescence rule based upon the stress state and microstructure geometry, the plastic limit-load criterion of Thomason (1990) has enabled void nucleation to be directly linked to fracture by removing the critical porosity as a material constant (Zhang 1996). The nucleation parameters in a Gurson-based material model can now be uniquely determined using notched tensile tests.

However, calibrating the nucleation parameters using a single-bound model like the GT yield criterion introduces an unavoidable bias because the parameters will reflect the formulation of the yield criterion. For example, void nucleation is used to effectively soften the Gurson (1977) model by increasing the porosity (lower nucleation stress/strain) to achieve coalescence at the experiment fracture strain. Conversely, the calibrated nucleation stress/strain would be higher in the Sun and Wang (1989) model to effectively stiffen the material by suppressing damage to avoid premature failure before the experimental strain is reached in the simulation. This bias can be mitigaged by using a dual bound approach since the nucleation parameter is identified using both bounds and thus captures the material behaviour within a band as shown in Fig. 2.34.

In this section, the dual bound approach to ductile fracture is used to identify the nucleation stress and strain parameters in AA5182 sheet using notched tensile specimens. Three specimen geometries were considered to identify the parameters over a range of stress states commonly found in a sheet metal forming process. The geometry of the microstructure is characterized from particle field measurements and implemented into the coalescence model to obtain physically reasonable porosities at fracture.

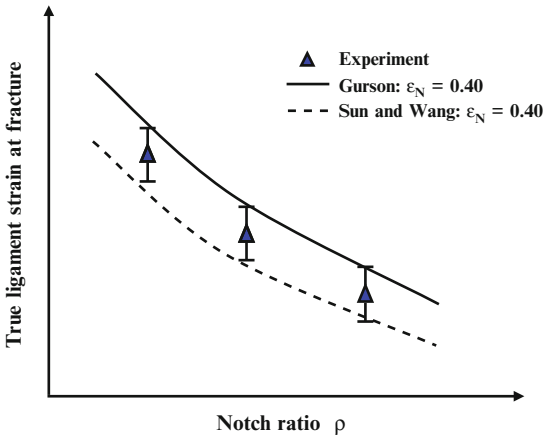

Fig. 2.34 Schematic representation of fitting the nucleation strain using the dual bound approach for notched tensile tests. In notched tensile specimens, a higher notch ratio corresponds to a higher stress triaxiality

2.12.1 Constitutive Modeling of Ductile Fracture

The dual bound constitutive models described in the previous sections were adopted with the exception of removing the critical porosity coalescence criterion and replacing it with a modified plastic-limit load criterion that eliminates the critical porosity as a material parameter. The same stress- and strain-controlled nucleation models of Chu and Needleman (1980) were again considered for this alloy, AA5182.

2.12.1.1 Void Coalescence

The PLL of Thomason (1990) was derived using an upper bound approximation to the material behaviour and should not be implemented into the lower bound SW model to ensure a consistent upper and lower bound analysis. This inconsistency is overcome by adopting the PLL model of Ragab (2004b) in Eq. (2.27) who replaced the plastic constraint factor derived by Thomason (1990) with the notch constraint factor of Bridgman (1952) for axisymmetric loading that was not derived using either upper or lower bound approximations. It is important to note that the use of a Thomason-based variant of the plastic constraint factor in the lower bound SW model is a minor issue and is only addressed in this work to provide a strict representation of the dual bound approach.

An additional consideration in selecting the Ragab variant of the plastic limit load in this application is because it has been shown to give much better fracture predictions than the variants of Pardoen and Hutchinson (2000) or Benzerga (2002) when applied to a large range of real materials (Ragab 2004b). While these variants of the plastic limit-load are accurate when compared to unit cell simulations, they tend to overpredict fracture in actual materials because the influence of secondary voids, shearing and other conditions are not considered. The Ragab model provides

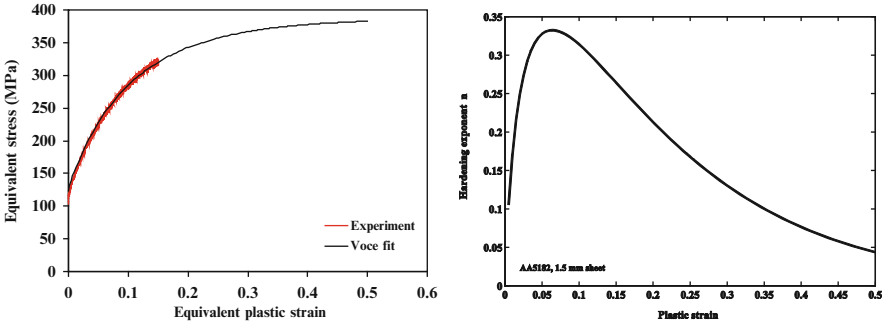

Fig. 2.35 Average experimental flow stress relation for AA5182 sheet with its Voce law representation (*left*) and the variation of the material hardening exponent obtained from the Voce law

a much lower plastic constraint condition and coalescence occurs sooner and is in better agreement with the experiments. From a physics perspective, the Pardoen and Hutchinson or Benzerga variants are the best but from an engineering perspective, the Ragab model is preferable. Coalescence occurs for spherical voids in the Ragab (2004b) PLL model when the condition in Eq. (2.27) is satisfied.

2.12.1.2 Material Properties

The flow stress relation for 1.5 mm thick AA5182-O sheet was determined using three standard tensile test specimens as shown in Fig. 2.35. The average flow stress response was expressed as a Voce hardening law (Voce 1948):

$$\bar{\sigma} = \sigma_s - \left(\sigma_s - \sigma_y\right) \exp\left[-\alpha(\bar{\varepsilon}^p)^\beta\right] \tag{2.34}$$

with $\sigma_y = 122.7$ MPa, $\sigma_s = 398.1$ MPa, $\alpha = 7.631$ and $\beta = 0.905$. AA5182 alloys exhibit different hardening regimes as shown in Fig. 2.35b where it initially resembles a high-strain hardening material with a peak hardening exponent of about 0.33 before the flow stress saturates and the matrix resembles that of a perfectly plastic material, $n \to 0$. The strain hardening parameter of AA5182 is computed at each stage during deformation using the relation

$$n = \frac{\bar{\varepsilon}^p}{\bar{\sigma}} \frac{d\bar{\sigma}}{d\bar{\varepsilon}^p} \tag{2.35}$$

The modulus of elasticity was estimated from the tensile tests to be 65.33 GPa and the Poisson's ratio was assumed to be the standard 0.33 for aluminum alloys.

Table 2.4 Controlling parameters in the Gurson and SW material models

f_o (%)	f_n (%)	f_f (%)	λ_{2o}	c	s_N (% ε_N, σ_N)	ε_N	σ_N
0.053	1.23	2.00	8.68	0.35	15	Identified parametrically	Identified parametrically

2.12.1.3 Selection of Damage-Based Material Parameters

The average area fraction of second-phase particles is 1.23 % (Chen 2004; Lievers et al. 2004; Orlov 2006) and is essentially damage-free with an initial porosity of 0.053 % (Orlov 2006) and failure porosity of 2 % (Chen 2004). The second-phase particles are essentially spherical with an average aspect ratio of 1.14 (Chen 2004) and exhibit significant clustering with an average particle spacing ratio, χ_p, of 0.588 (Butcher and Chen 2009b, c). The initial unit cell aspect ratio must be determined from the particle distribution to characterize the microstructure in the coalescence model. Since voids are nucleated at the particles, the initial unit cell geometry for a periodic arrangement of cubic unit cells can be obtained from the particle field data. Therefore, the aspect ratio of the cubic unit cell containing a spherical particle is determined to be $\lambda_{2o} = \frac{\pi}{6}\frac{\chi_p^3}{f_p} = 8.68$. It is assumed that area-based estimates of the microstructural variables are reasonable approximations to the volume-based measurements used in the damage-based constitutive model.

The only remaining parameters are related to void nucleation. Typically, nucleation in this alloy has been assumed to obey the strain-controlled model in Eq. (1.5) with nucleation strains reported in the range of 0.20–0.70 (Lievers et al. 2004; Butcher et al. 2006; Chen and Worswick 2008; Butcher and Chen 2009a, b, c) and nucleation stress of 440–500 MPa (Butcher et al. 2006). The standard deviation of the nucleation stress/strain in Eqs. (1.5) and (1.7) is assumed to be 15 % the nucleation stress or strain (Chen 2004; Orlov 2006). The nucleation stress and strain will be determined parametrically through calibration with the tensile test data (Table 2.4).

2.12.2 Notch Tensile Test Experiment

Notched tensile specimens of 1.5 mm thick AA5182 sheet with a notch radius, R, of 3 mm and gage length, L, of 12.5 mm were tested to failure in an Instron 1,332 testing machine with a crosshead velocity of 0.03 mm/s. The notch ligament length was varied to achieve various stress states and was characterized using the notch ratio defined as

$$\rho = \frac{2R}{w} \tag{2.36}$$

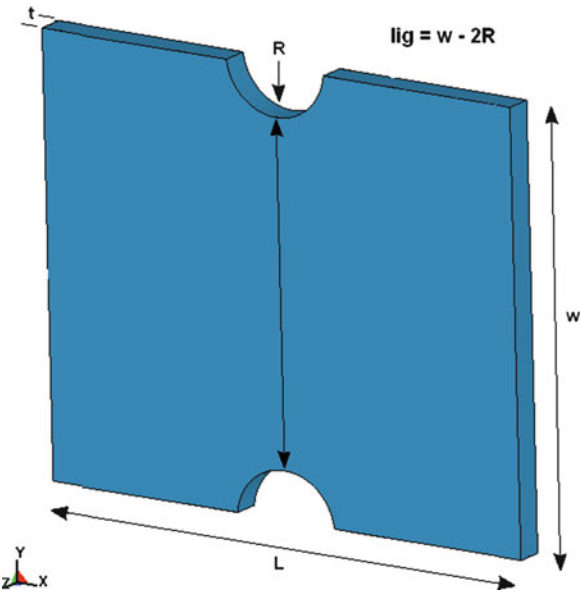

Fig. 2.36 Geometry of a typical notched tensile sheet specimen. The loading and rolling directions are collinear with the x-axis. The specimen is symmetric about the x, y and z axes

where w is the sample width. The notch ratios considered were 0.25, 0.33 and 0.50 and correspond to ligament lengths of 18, 12 and 6 mm. A total of six specimens for each notch ratio were tested to failure. All of the samples were fabricated with the loading direction aligned with the rolling direction of the sheet. The typical specimen geometry is presented in Fig. 2.36.

Notched tensile specimens are used to alter the stress state in the ligament and force localization to occur within the ligament. Two experimental fracture strains are used in the calibration of the nucleation models: (i) the ligament strain, $\varepsilon_{\mathrm{lig}_f}$, and (ii) the axial strain $\varepsilon_{\mathrm{a}_f}$. The ligament strain is adopted because it is representative of deformation where the specimen fractures. The axial strain at failure is used to provide a metric that is independent of the fractured region and representative of bulk deformation. The axial and ligament strains at fracture are defined as

$$\varepsilon_{\mathrm{a}_f} = \ln\left(\frac{L_f}{L_o}\right) \quad \varepsilon_{\mathrm{lig}_f} = \ln\left(\frac{\mathrm{lig}_f}{\mathrm{lig}_o}\right) \tag{2.37–2.38}$$

where the initial ligament length is $lig_o = w - 2R$. The axial strain at failure is recorded at the appearance of a macro-crack at the notch root and not final failure since the objective of the finite-element models is to predict the formation of a macro-crack and not the subsequent tearing process of the ligament. Finite-element modeling of this process would require additional modelling considerations such as the use of cohesive elements.

Tensile specimens with notch ratios of ~1/3 or lower will exhibit visible cracking at the notch root prior to fracture as shown in Fig. 2.37. The onset of cracking at the

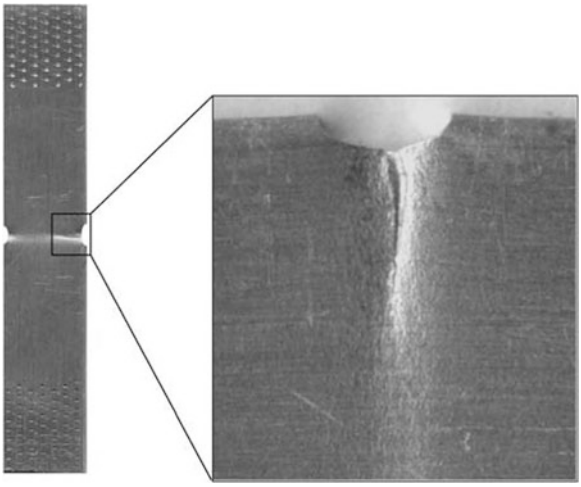

Fig. 2.37 Crack initiation at the notch root in a 1.5 mm thick AA5182 tensile specimen with a notch ratio of 0.125 and notch radius of 1 mm

notch root is readily identified from the experimental load-elongation curve as the appearance of the crack corresponds to an abrupt load drop as shown in Fig. 2.38.

2.12.3 Finite-Element Model

Due to symmetry, only one-eighth of the geometry is represented in the finite-element model. A velocity boundary condition is applied to the free-end of the specimen. A sinusoidal velocity profile is used to limit inertial effects with a peak velocity corresponding to a strain rate of 100 s^{-1}. As shown in Fig. 2.39, the tensile specimens were modeled with eight-node constant stress brick elements with 24,000, 18,000 and 12,000 elements for notch ratios of 0.25, 0.33 and 0.50, respectively. The mesh sensitivity for each notch ratio was negligible.

2.12.4 Identification of the Fracture Strains

The finite-element simulation is terminated at the onset of element deletion signifying localized necking and the onset of failure. The satisfaction of the post-coalescence criterion in Eq. (2.24) triggers element deletion in the finite-element model with widespread fracture of the specimen occurring at the onset of element deletion. The resulting ligament strain and elongation-to-failure are then obtained from the finite-element model and compared with the experiment values. The optimal nucleation parameter is identified when the formability band best captures the material behaviour over the range of notch ratios. Since the objective is to

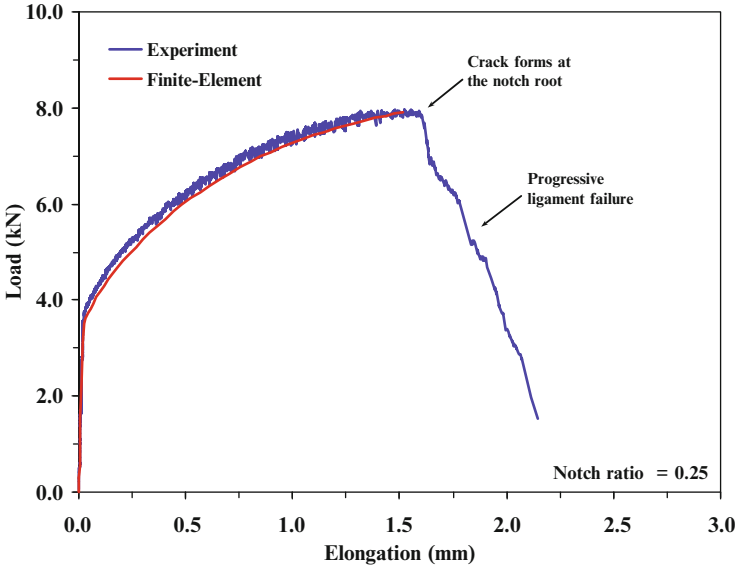

Fig. 2.38 Comparison of the average experimental and predicted load-curve for an AA5182 notched tensile specimen using the GT model. The predicted load-curve using the SW model is not presented because there was no visible difference in the response. The insensitivity of the load curve to the damage model is due to the small initial porosity and the fact that significant damage evolution occurs in a very small region of the notch. Tensile samples with a smaller notch ligament and a higher porosity at fracture would result in a larger difference in the predicted load-displacment responses

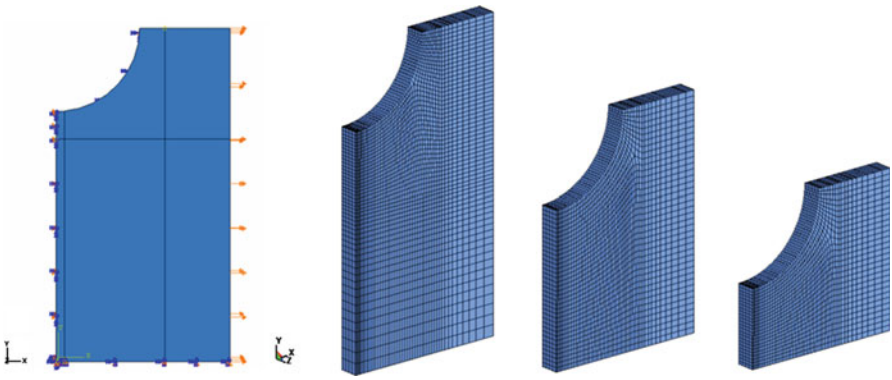

Fig. 2.39 Typical boundary conditions of the one-eighth FE model of the tensile specimens and the respective meshes for notch ratios of 0.25–0.50

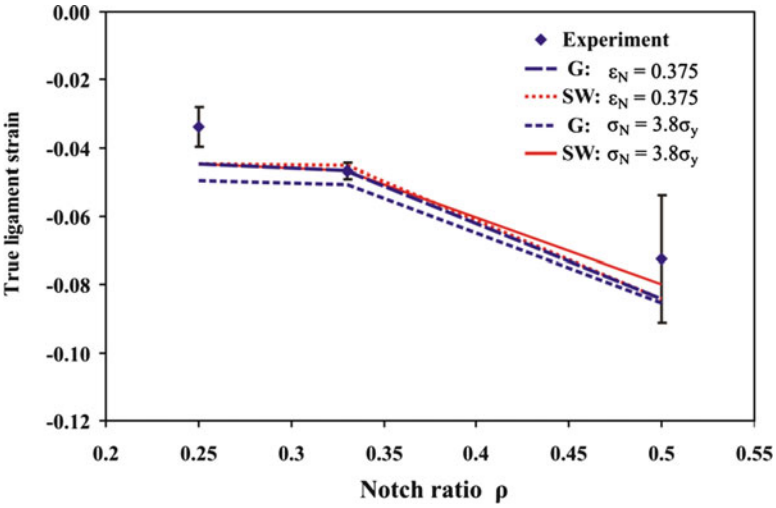

Fig. 2.40 Comparison of the experimental and numerical true ligament strains determined by the Gurson and SW models using stress- and strain-controlled nucleation for various notch ratios. The experimental true ligament strain is presented as a 95 % confidence interval

capture the fracture behaviour within a band, the experimental fracture strains are expressed using two-tailed 95 % confidence intervals.

2.12.5 Results and Discussion

2.12.5.1 Ligament Strain and Elongation-to-Failure

A parametric study was conducted to calibrate the void nucleation models in the Gurson and SW material models using notched tensile test data. Stress- and strain-controlled nucleation models with values of $\sigma_N = 3.8\sigma_y$ (466.26 MPa) and $\varepsilon_N = 0.375$ can provide good agreement with the experimental ligament strain and elongation-to-failure as shown in Figs. 2.40 and 2.41, respectively. The nucleation stress is in good agreement with the range of 440–500 MPa suggested by Butcher et al. (2006). The nucleation strain is also reasonable as Butcher and Chen (2009a, b, c) and Orlov (2006) suggested values of 0.42 and 0.30 in uniaxial tension. The performance of the dual bound approach is sensitive to the assumed nucleation model. A single bound model is sufficient if strain-controlled nucleation is adopted since the difference in the fracture predictions of the Gurson and SW models is marginal. The opposite behaviour is observed using stress-based nucleation which yields a meaningful formability band that captures the material behaviour and highlights the benefits of the dual bound approach.

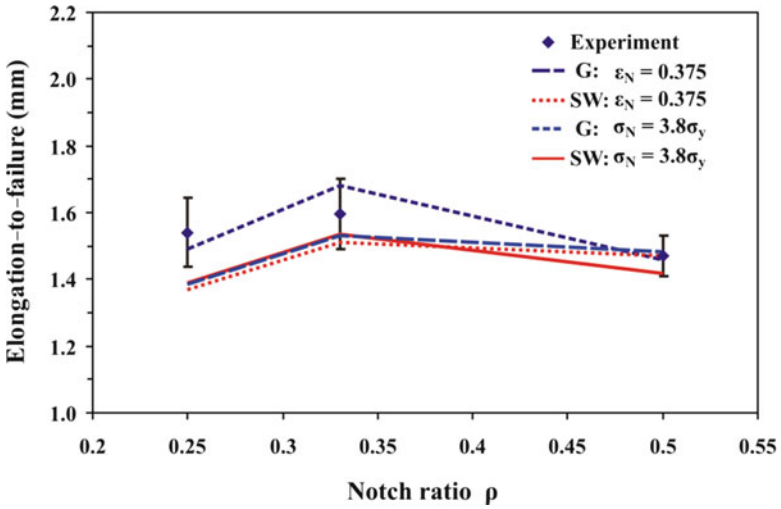

Fig. 2.41 Comparison of the experimental and numerical elongation-to-failure determined by the Gurson and SW models using stress- and strain-controlled nucleation for various notch ratios. The experimental elongation is presented as a 95 % confidence interval

2.12.5.2 Load-Elongation

In addition to providing good agreement with the ligament strain and elongation-to-failure, both the Gurson and SW models provide excellent agreement with the experimental load-elongation curves for each notch ratio as shown in Fig. 2.42. A crack originated at the notch root for notch ratios of 0.25 and 0.33 which then propagated throughout the ligament leading to fracture. The onset of cracking in these specimens is accompanied by a sudden load drop as seen in Fig. 2.42. Fracture occurred abruptly for a notch ratio of 0.50 with no visible cracks at the notch root.

2.12.5.3 Fracture Location

The predicted fracture locations and porosity contours obtained using both stress and strain-controlled nucleation are presented in Figs. 2.43 and 2.44, respectively. Damage development in the stress-controlled nucleation model mimics the stress triaxiality distribution and damage occurs over a larger area compared to the strain-controlled nucleation model. The fracture locations for both nucleation models are in good qualitative agreement with the experiment as fracture originates at the notch root for $\rho = 0.25$ and 0.33. The failure location for $\rho = 0.50$ is unknown since the ligament abruptly fails with no visible cracking at the notch root.

Void damage is highly localized in the strain-controlled nucleation model as the plastic strain is highest at the notch root for each notch ratio. Void nucleation occurs

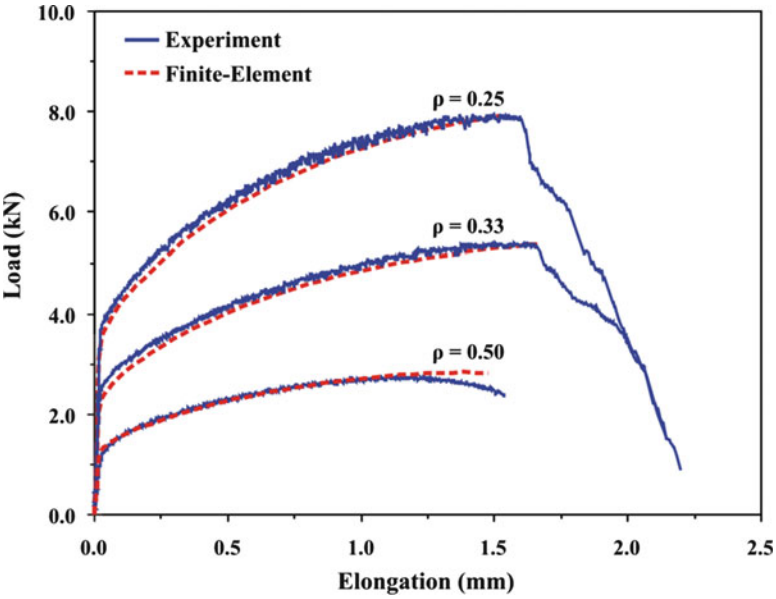

Fig. 2.42 Comparison of the experimental and numerical load-elongation curves for each notch ratio. The finite-element results were obtained using the Gurson model with a nucleation stress of $\sigma N = 3.8\sigma_y$. The load-displacement curves for the SW model are not shown for clarity (Reprinted with permission from Butcher and Chen (2011). Copyright: Elsevier)

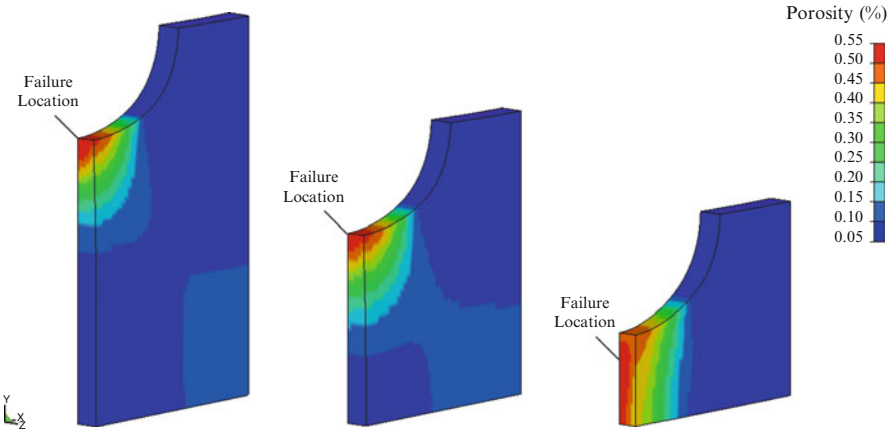

Fig. 2.43 Contours of porosity prior to fracture for notch ratios of 0.25, 0.33 and 0.50 (*left* to *right*) obtained using the Gurson model with stress-controlled nucleation, $\sigma_N = 3.8\sigma_y$. The general contours are similar using the Sun and Wang model but the porosity is higher (Reprinted with permission from Butcher and Chen (2011). Copyright: Elsevier)

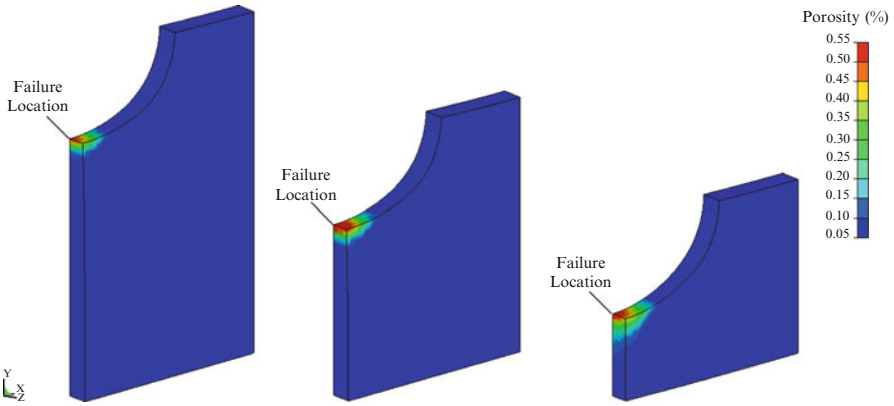

Fig. 2.44 Contours of porosity prior to fracture for notch ratios of 0.25, 0.33 and 0.50 (*left* to *right*) obtained using the Gurson model with strain-controlled nucleation, $\varepsilon_N = 0.375$. The contours are similar using the Sun and Wang model (Reprinted with permission from Butcher and Chen (2011). Copyright: Elsevier)

over a wider area using stress-controlled nucleation since it is dependent upon the flow stress (plastic strain) and hydrostatic stress. While the plastic strain is highly localized at the notch root, the peak hydrostatic stress moves from the notch root for $\rho = 0.25$ to the center of the ligament for $\rho = 0.50$. Void nucleation occurs over a larger region as it is the sum of these two distributions.

Overall, the range for the stress triaxiality (ratio of hydrostatic to effective stress) is not large among the different geometries. The stress triaxiality in the center of the specimen varies from 0.33 to 0.60 for notch ratios of 0.25 to 0.50. Future work could consider using both sharp and circular notches to obtain a larger range of stress triaxiality and assess the transferability of the parameters to these stress states.

2.12.5.4 Void Damage

The sensitivity of the dual bound approach to the nucleation model is caused by the different porosity profiles that develop in the material. The porosity histories obtained for a notch ratio of 0.33 using both nucleation models are presented in Fig. 2.45. The histories are similar for the other notch ratios. Void nucleation using the stress-based model exhibits progressive nucleation throughout deformation as the stress state evolves. Stress-based nucleation is related to both the hydrostatic stress and flow stress (function of plastic strain). Unlike the strain-controlled nucleation model, nucleation can occur at an earlier stage of deformation in a region where the plastic strain is lower but where the hydrostatic stress is significant. The ability to nucleate voids earlier in the deformation process leads to a larger contribution of void growth. A larger void growth component highlights the difference between the Gurson and SW models since voids grow faster in the softer

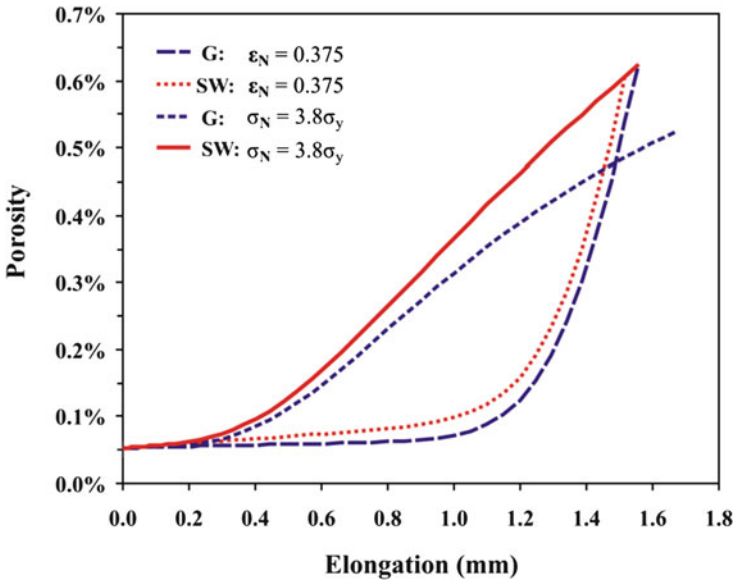

Fig. 2.45 Damage evolution within the first element-to-fail for a notch ratio of 0.33 using both *upper* and *lower* bound models and stress and strain-controllednucleation rules. The trends are similar for the other notch ratios

SW model and slower in the more rigid Gurson model. Consequently, the fracture strains predicted by the Gurson and SW models diverge and define a formability band.

In the strain-based nucleation model, void nucleation is negligible until the latter stages of deformation where rapid nucleation occurs leading to sudden fracture. This burst of nucleation overshadows any difference in the porosity between the Gurson and SW models due to void growth and fracture occurs at similar strains. In this case, coalescence is nucleation driven with marginal void growth.

The porosities at the onset of coalescence are physically reasonable which suggests the microstructure characterized using the particle distribution is representative of the material in the coalescence model. The porosity at coalescence ranges from about 0.5 to 0.7 % which is in general agreement with the experimental results of Smerd et al. (2005) who reported porosities near the fracture surface of tensile specimens of 0.5–1 % for various strain rates. A detailed analysis of the AA5182 microstructure in the notch tensile tests is discussed in Chap. 7 in regards to damage percolation modelling. Overall, both stress and strain-controlled nucleation models can be adopted for AA5182 sheet. It is important to mention that the Gurson and SW models are approximate yield criteria that are based on many simplifying assumptions and the calibration of the nucleation models will artificially correct for some of their deficiencies. The present results should only be considered valid for these specific nucleation rules and are dependent upon the coalescence model and its parameters.